Journal of Energy Storage 99 (2024) 113267

Contents lists available at ScienceDirect

Journal of Energy Storage

journal homepage: www.elsevier.com/locate/est

Research papers

High performance quasi-solid-state supercapacitor based on activated carbon derived from asparagus waste

Niyaz Ahmad [a,b], Alessia Rinaldi [a,b], Michele Sidoli [a,b], Giacomo Magnani [a,b,*], Alberto Morenghi [a,b], Silvio Scaravonati [a,b], Vincenzo Vezzoni [a,b], Lorenzo Pasetti [a,c], Laura Fornasini [a,c], Francesca Ridi [d], Chiara Milanese [e], Mauro Riccò [a,b], Daniele Pontiroli [a,b]

[a] Nanocarbon Laboratory, cIDEA & Department of Mathematical, Physical and Computer Sciences, University of Parma, Parco Area delle Scienze 7/A, 43124 Parma, Italy
[b] GISEL National Centre of Reference for Electrochemical Energy Storage Systems, INSTM National Interuniversity Consortium of Materials Science and Technology, Via Giusti 9, 50121 Firenze, Italy
[c] Department of Mathematical, Physical and Computer Sciences, University of Parma, Parco Area delle Scienze 7/A, 43124 Parma, Italy
[d] Department of Chemistry "Ugo Schiff" & C. S. G. I., University of Florence, Via della Lastruccia, 3, 50019 Sesto Fiorentino, FI, Italy
[e] Pavia Hydrogen Lab, Department of Chemistry & C. S. G. I., University of Pavia, Viale Taramelli 16, 27100 Pavia, Italy

ARTICLE INFO

Keywords:
Gel polymer electrolyte (GPE)
Ionic liquid
Supercapacitor
Biomass waste
Activated carbon

ABSTRACT

Supercapacitors with carbon electrodes derived from biomass and utilizing gel polymer electrolytes are currently a focal point in the development of highly efficient, environmentally friendly, and cost-effective energy storage devices. In this study, we present porous activated carbon derived from asparagus waste, prepared through chemical activation with $ZnCl_2$ followed by physical activation with CO_2, as a high-performance electrode material for supercapacitors. The performance of electrodes has been discussed in comparison with supercapacitors employing both gel polymer electrolytes and conventional liquid electrolytes i.e. 7 M KOH. The flexible film of the gel polymer electrolyte exhibits noteworthy characteristics, including a high ionic conductivity of ~6.3 mS cm^{-1}, and a high electrochemical stability window of ~4.5 V. Supercapacitors prepared with this gel polymer electrolyte outperform supercapacitors with liquid electrolytes thanks to a broader electrochemical stability window, showing optimal charge-discharge performance, a specific capacitance of 160 F g^{-1}, a specific energy of 31 Wh kg^{-1}, and an effective power of 0.56 kW kg^{-1}. The superior rate performance is demonstrated by powering a LED for a substantial duration, highlighting the exceptional capabilities of the system. Additionally, the supercapacitor employing the gel polymer electrolyte displays an extended stability, sustaining approximately 10,000 charge-discharge cycles with only a modest initial fading of ~16 % in specific capacitance and maintaining a high coulombic efficiency of ~100 %.

1. Introduction

Supercapacitors, also known in literature as ultracapacitors or electric double layer capacitors (EDLCs), are electrostatic charge-storage mechanism-based devices with numerous applications in electronic, engineering, and medical devices as well as in electric and hybrid vehicles (HEVs) [1–3]. EDLCs possess higher power density compared to Li-ion batteries, but lower energy density. Both the electrodes and the electrolyte, having fast ion movement, contribute to the high power capabilities of supercapacitors, while the large surface area and unique electrochemical characteristics of the electrodes contribute to the high specific energy [4–10]. Even though batteries have been used for charge storage applications for a long time thanks to their high energy storage capabilities, current demand is related to high-rate energy delivery, environmental friendliness, cost, size, and weight, characteristics adequately provided by supercapacitors [2]. Many carbonaceous materials are generally used as electrode materials in supercapacitors due to their many appealing characteristics, mainly consisting of their low cost and ease of availability, high conductivity, large surface area, and resilience to corrosion. Examples of these materials include activated

* Corresponding author at: Nanocarbon Laboratory, cIDEA & Department of Mathematical, Physical and Computer Sciences, University of Parma, Parco Area delle Scienze 7/A, 43124 Parma, Italy.
E-mail address: giacomo.magnani@unipr.it (G. Magnani).

https://doi.org/10.1016/j.est.2024.113267
Received 18 January 2024; Received in revised form 1 July 2024; Accepted 4 August 2024
Available online 12 August 2024

carbons (ACs), carbon nanofibers/aerogels/flakes, graphene, and carbon nanotubes (CNTs) [11–20]. Across the world, efforts are still being made to modify electrodes and electrolytes to increase the energy density of such energy storage devices [21]. Recent findings claim that in order to increase the energy density of supercapacitors, electrolytes are also crucial in the production of high-performance supercapacitors [22–24].

Waste biomass resources are reportedly used to manufacture AC electrodes for supercapacitors, in order to make affordable and "green" energy storage devices [25]. Biopolymers mostly made of celluloses, lignin and hemicelluloses are commonly used as raw materials for ACs, and value-added products for a variety of expanding carbon-based applications can be obtained from them [3]. Studies indicate that biochar derived from biomass precursors (i.e. manure, wood residue, and agricultural waste) through pyrolysis is characterized by a hierarchical porous structure, suitable for supercapacitors [26,27]. Coconut shells, coffee grounds, almond shells, tea leaves, rice husks, poplar wood, poultry litter, and other biomass-based materials can be used to synthesize ACs for high-performance electrodes in EDLCs [28–34].

AC is typically obtained by pyrolysis of waste materials, possibly followed by various chemical or physical activation steps, which allow tuning the porosity of materials [3]. According to literature, the presence of large cations and/or anions restricts the use of typical highly porous AC electrodes since those ions either cannot fit inside smaller pores or have limited diffusion at the required scan rates [16,35]. Hence, in order to obtain properly sized pores, physical activation (such as steam or CO_2), capable of producing pores with a wide range of sizes, is indicated [36]. In general, higher microporosity and substantial amount of mesoporosity present in the carbon electrodes promotes greater performance of the EDLCs [25]. In order to tailor various properties including porosity, microstructure, and surface area, carbon materials are typically chemically activated, and subsequently physically activated [25]. Typically, chemical activation methods involve different activating reagents, such as H_3PO_4, $ZnSO_4$, $ZnCl_2$, K_2CO_3, Na_2CO_3, KOH, NaOH, $CaCl_2$ [28,37]. In comparison to physical activation, chemical activation typically occurs at lower temperatures, requiring less energy and displaying higher yield [3].

In this work, a highly porous activated carbon (AC) was synthesized from asparagus waste. Regarded as the "king of vegetables," asparagus ranks among the ten most well-known foods in the world [38,39]. It is widely consumed because of its pleasant flavor and comparatively higher quantity of vitamins, protein, and amino acids than other fruits and vegetables [38,39]. Asparagus has traditionally been utilized both as food and as a medicine. Recently, there has been an upsurge in demand for asparagus, which is now widely grown around the world [38]. China is the world's largest producer of asparagus, and its asparagus cultivation area has expanded by 46.5 % between 2001 and 2011, from 901,538 hm^2 to 1,320,597 hm^2 [38]. A total of 7,252,903 tons of asparagus were produced in China in 2011, making up 88.0 % of the total world production [38]. In Europe, Germany is the largest producer of asparagus, and >100,000 tons of special white asparagus are harvested during the "Spargelzeit" or asparagus season [40]. After Germany, Spain is the second-largest producer of asparagus in Europe, producing and collecting >21 % of the continents total production [41]. According to the Spanish Ministry of Agriculture, Fisheries, and Food (2020), asparagus is one of the most popular stem vegetables farmed in Spain [42,43]. In 2018, its national production amounted to nearly 68 thousand tons, or 4 % of all vegetables grown [43]. As only the young shoots of the asparagus are edible, an enormous amounts of asparagus stems are left as byproduct of the asparagus life cycle [38,42]. As a lignocellulosic biomass resource, the asparagus stem can be used as potential feedstock for the application of biomass-derived carbon based electrochemical energy storage devices.

Supercapacitors commonly employ liquid electrolytes (LEs), which can be either aqueous or organic. LEs are the most used ones because they are inexpensive, show good ionic conductivity, and are easy to manufacture [44–46]. However, when employed in devices, LEs have several drawbacks, including leakage, corrosion, limited transportability, a limited electrochemical stability window for aqueous electrolytes, rapid volatility, and flammability of organic electrolytes [45,47]. The quick volatility and flammability of LEs can be reduced or eliminated by using ionic liquids (ILs) in pure form or their salt solutions, although a few other problems still exist [45,48–51]. A particular class of electrolytes, known as gel polymer electrolytes (GPEs), is a promising substitute for LEs because of their excellent interfacial compatibility with electrodes, strong ionic conductivity that is almost equal to that of LEs, and great flexibility. In general, host polymers like PEO, PVA, PVdF, PVdF-HFP, are used to trap LEs to form GPEs [52]. Incorporation of ionic liquid in GPEs have proven an excellent choice for GPEs to have outstanding thermal stability, broad electrochemical stability window, and corrosion- or leakage-free characteristics [53]. Conductivity and other electrochemical properties of GPEs can be further improved by adding Li, Mg, and Na ion salts.

In this work, we report the analysis of AC derived from asparagus waste as high performance carbon electrode for supercapacitors. The synthesis of highly porous ACs involved the activation of asparagus waste using varying amounts of the chemical activating agent $ZnCl_2$, which was then followed by physical activation with CO_2. The AC powder was characterized via BET surface area and porosity analysis, XRD, SEM-EDS and Raman spectroscopic measurements.

AC powder was tested as high-performance capacitive electrode with aqueous electrolyte (KOH) and high working voltage window GPE in two electrode configurations. Through many cycles of galvanostatic charge-discharge (GCD), cyclic voltammetry (CV) and electrochemical impedance spectroscopy (EIS), the relative performance of supercapacitors has been evaluated. The results of the experiment demonstrate the higher performance of supercapacitors made using liquid/gel electrolyte, in terms of specific capacitance, specific power and energy upon cycling.

2. Experimental

2.1. Materials and device preparation

2.1.1. Preparation of ACs

The graphical representation of AC powder preparation is shown in Fig. 1. Stems obtained from organic asparagus cultivation in a private yard in Pavia province were cut in pieces and dried in a furnace for 8 h at 45 °C. Subsequently, the dried pieces were washed with deionized (DI) water followed by drying and mortar crushing to obtain a fine dry powder. $ZnCl_2$ (Merck KGaA, 99 % purity) was employed as a "green" activating agent. To perform the activation of the asparagus waste, $ZnCl_2$ was dissolved in DI water, then raw asparagus waste powder was mixed in both asparagus:$ZnCl_2$ 1:2 and 1:3 ratios, to carry out different chemical activations. After 6–7 h of constant stirring, the $ZnCl_2$-biomass suspension was dried overnight at about 70 °C in an oven. The dehydrated powders were moved into an alumina boat and heated to approximately 800 °C, with a steady flow of Argon gas. The heating process was carried out at a rate of 5 °C per minute. After the furnaces temperature reached 800 °C, the Ar gas flow was changed with CO_2 gas, and maintained for two hours to allow the CO_2 physical activation. It is in fact known that an enlargement in ACs pore size can be achieved by CO_2 physical activation at high temperature [54]. After 2 h at 800 °C under continuous CO_2 gas flux, the atmosphere was again switched to Ar, and the furnace was allowed to naturally cool to room temperature. The carbonaceous product was then recovered and washed with DI water to remove zinc and chloride ions from the samples, and subsequently filtrated on a Buchner funnel. The sample was then recovered and suspended in a 1 M HCl (Merck KGaA, 37 % water solution) solution to remove all possible contaminants. The HCl residues were then removed by washing with DI water until pH was neutral. Lastly, the AC products were vacuum dried for 12 h at a temperature of 60 °C and then

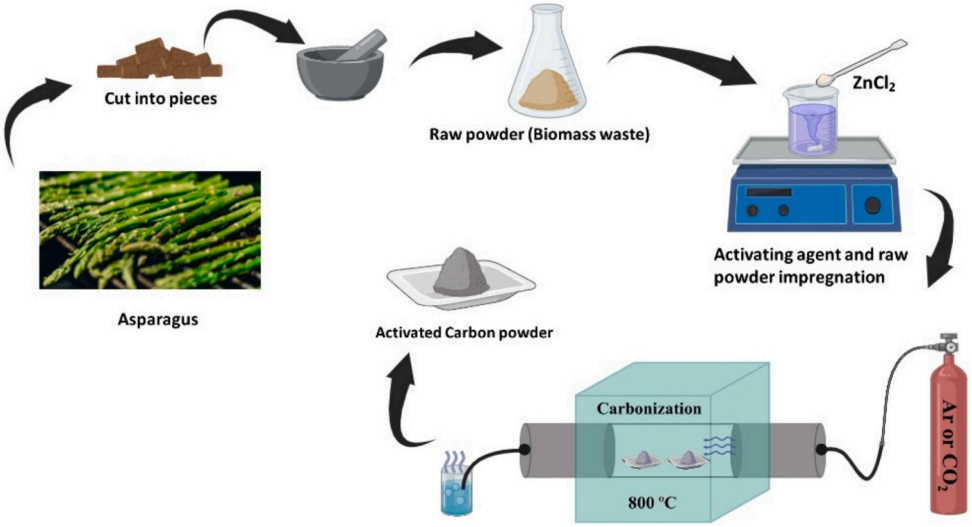

Fig. 1. Preparation steps of Activated carbon form Asparagus waste.

characterized and used as electrode material of a supercapacitor.

The carbon electrodes for supercapacitors were obtained by mixing the AC with the conductive additive (carbon black, TIMCAL Super-P) and polymer binder poly(vinylidene fluoride-*co*-hexafluoro propylene (PVdF-HFP), (purchased from Merck KGaA, Mw ~ 400,000). The conductive additive was added to obtain a good electrical conductivity, and to increase electron-transfer, due to the catalytic capability of carbon black [21]. At first, a smooth slurry was made by mixing AC (80 wt %) in a mortar with carbon black (TIMCAL Super C65, 10 wt%) and PVdF-HFP (10 wt%), and adding a proper amount acetone (Merck KGaA, HPLC grade, ≥99.8 %). The resulting slurry was then drop-casted onto circular flexible graphite discs (16 mm diameter). Before using the obtained electrodes in the fabrication supercapacitors, they were vacuum dried for 8–12 h at a temperature of about 80 °C. The resulting dried active material mass on the disks was ranging from 0.88 to 1.1 mg cm^{-2}.

2.1.2. Preparation of electrolytes

Two different electrolytes, namely 7 M KOH (A.C.E.F., 99 %) aqueous electrolyte, and lithium salt/ionic liquid integrated gel polymer electrolyte (GPE), were used to investigate the capacitive performance of AC powders. In order to prepare ILGPE, solid pellets of the host polymer PVdF-HFP (1 g) were first dissolved in 20 ml of acetone while being constantly stirred for 12 h. To fully immobilise IL in the host polymer, 4 g of 1 M lithium bis(trifluoromethanesulfonyl)imide (LiTFSI) (Merck KGaA, anhydrous, 99.99 %) in 1-butyl-1-methylpyrrolidinium bis(trifluoromethylsulfonyl)imide (BMPTFSI) (Merck KGaA, >99 %, <500 ppm H_2O) were added to the PVdF-HFP solution. The mixture was then stirred again for 8–10 h. GPE film was formed by gradually allowing the evaporation of acetone after pouring PVdF-HFP/1 M LiTFSI in BMPTFSI into a glass petri dish. A free-standing, highly flexible GPE, with thickness ~ 400–500 μm, was obtained in four to five days following the full evaporation of the acetone. The gel film was kept in a dry environment for further use, to prevent moisture and contamination. In the preparation of the GPE all steps have been performed at room temperature (27 °C) in ambient conditions.

Ionic conductivity and electrochemical stability window (ESW) have been evaluated in order to analyse the electrochemical performance of the GPE. The cell configuration SS|GPE-film|SS and SS|GPE-film|Ag has been selected to measure the ionic conductivity and ESW of the GPE film, respectively. SS was the stainless-steel sheet and Ag was silver foil. In the SS|GPE-film|Ag configuration, SS and Ag acted respectively as a working and counter/reference electrode.

2.1.3. Fabrication of EDLCs

Supercapacitors were assembled with GPE and liquid electrolyte (7 M KOH). The GPE/liquid electrolyte (glass microfiber separator soaked in aqueous electrolyte i.e. 7 M KOH) was placed between the two symmetric carbon electrodes. The GPE/glass fiber (Whatman 1825 borosilicate glass microfiber, 0,7 μm) separators were cut circularly of appropriate size for electrodes slightly larger than the two symmetric electrodes to avoid the sort-circuit between the two symmetric electrodes. Therefore, the carbon electrodes and GPE films/liquid electrolyte were stratified in the geometry of AC| electrolyte |AC. The EDLC cells were fabricated in the following configurations:

Cell-1: AC | GPE-film | AC.
Cell-2: AC | 7 M KOH | AC.

Both the cells were electrochemically analysed by EIS, GCD and CV in the two electrode configurations. An alternate current signal with an amplitude of 10 mV was applied in the frequency range from 10^5 Hz to 10 mHz to perform the EIS measurements. A 1010E Interface Potentiostat (Gamry Instrument, USA) electrochemical workstation was used for EIS and CV measurements, while the Landt CT2001A charge-discharge unit was employed for GCD and cyclic tests.

2.2. Material characterization techniques

2.2.1. Structural and morphological characterization

The analysis of nitrogen adsorption and desorption was carried out at liquid nitrogen temperature with a 3Flex analyzer (Micromeritics, Norcross, Georgia, USA). Before the measurement was performed, samples underwent pretreatment in nitrogen flux (4 h at 120 °C) using a FlowPrep apparatus (Micromeritics, Norcross, Georgia, USA), and then degassed in situ (2 h at 120 °C under vacuum), directly on the 3Flex ports: these steps enabled the removal of impurities and humidity from the surface. BET (Brunauer Emmett Teller) method was employed to estimate the total specific surface area of the samples, upon verification that the measurements met the Rouquerol criteria [55], while t-plot analysis was performed to calculate the external specific surface area, utilizing the carbon black Statistical Thickness Surface Area (STSA) equation [56].

Both the BJH (Barrett-Joyner-Halenda) protocol and the Non-Local Density Functional Theory (NL DFT) calculation were used to investigate the pore size distribution. The NL-DFT calculation was performed using the NLDFT(SD3), N2–77-Carbon Slit model, specific for carbon materials with infinite slit geometry [57,58].

The examination of the structure of ACs and the identification of impurities were conducted utilizing Powder X-ray diffraction (PXRD) analysis. PXRD assessments were carried out on powdered AC samples utilizing a Bruker D2 Phaser diffractometer, operating in Bragg-Brentano geometry with a 10°- 60° 2θ range. The diffractometer operated with a copper filament (Cu Kα). The sample was placed onto a zero-background specimen holder, which was spun during the measurement to reduce preferred orientations, and a LYNXEYE detector was employed. Data were analysed with GSAS-II and Match! software.

The investigation of AC structures also involved micro-Raman analysis, executed using a confocal Horiba Jobin Yvon LabRam micro-spectrometer (HORIBA Scientific, Kyoto, Japan) featuring a 300 mm focal length. Excitation was achieved using the 473.1 nm line of a double Nd:YAG laser, spanning a spectral range of approximately 100 to 2000 cm^{-1}. The calibration of the system was performed using the silicon Raman peak (at 520.6 cm^{-1}) as a reference. The apparatus was equipped with an Olympus BX40 microscope (Olympus, Tokyo, Japan), a grating with 1800 grooves/mm, a motorized XY stage, and a silicon CCD cooled by Peltier module. Employing a ULWD 50× objective, the laser beam was focused onto the sample, and scattered photons were collected. System calibration incorporated the use of density filters to diminish the potential beam damage by the laser, thereby preventing adverse thermal effects on the carbon-based sample. Spectra were recorded with standard exposures of 30 s, accumulating a minimum of 4 times each. Fluorescent background subtraction was executed through a polynomial curve and AC contributions in the spectra were deconvoluted using Gaussian-Lorentzian curves.

Morphological and elemental analysis of the ACs were performed by means of a Hitachi TM4000Plus II tabletop scanning electron microscope equipped with AztecOneXplore EDS detector. Loose powders have been laid on carbon tape and glued on the sample holders. Typical accelerating voltage of electrons was set at 15 kV and the morphology analysis was performed analyzing both secondary and backscattered electrons, to get a more precise rendering of the sample surface.

2.2.2. Electrochemical characterization

A Gamry electrochemical workstation, stated above, was used to perform electrochemical measurements. The analyses were carried out on both the as-prepared electrolyte and the final assembled device i.e., EDLCs. EIS measurements were carried out between 10 mHz to 10^5 Hz frequencies, by applying the AC signal of 10 mV. Linear Sweep Voltammetry (LSV) was conducted in a two-electrode system, applying a 10 mV s^{-1} constant rate, to evaluate the GPE stability window. The CV tests of EDLCs were carried out trying different voltage ranges, to test the electrolyte window (0 to 2.5 V for GPE based EDLC and 0 to 1.3 V for liquid electrolyte based EDLC) at a constant 10 mV s^{-1} scan rate. Then, the optimized voltage was kept constant and different scan rates were tested (from 10 to 300 mV s^{-1}).

GCD analysis was performed to measure the capacity, the efficiency and the capacity retention of the supercapacitors produced with asparagus-derived activated carbon. The measurements were performed using a Landt CT2001-A and a Neware BTS-4008 (5 V50 mA) battery testing system. GCD measurements were carried out both at constant current (chronopotentiometry) and at constant voltage. In order to optimize the working voltage ranges, the EDLCs were cycled at different voltages (0 to 2.5 V for GPE based EDLC and 0 to 1.3 V for liquid electrolyte based EDLC) at constant current 1 A/g. Thereafter, the EDLCs were cycled at the optimized voltage, using different current densities. The EDLCs were also cycled at constant current density for 10,000 cycles, using 1 mA cm^{-2} current.

3. Results and discussion

3.1. Study of AC

3.1.1. Sorption analysis

The isotherms obtained by nitrogen sorption analysis are reported in Fig. 2 (A). Their shape is typical of complex porous systems, which are mainly microporous, but with a mesoporous portion, as testified by the presence of the small hysteresis. According to the IUPAC classification [59], the shape of the hysteresis can be categorized as H3, which is indicative of a complex system of pores, mostly slit-like. The analysis of the curve obtained on Asparagus:$ZnCl_2$ (1:2) gave a BET specific surface area of 1516 m^2/g and pore volume of 1.24 cm^3/g, while the analysis of Asparagus:$ZnCl_2$ (1:3) resulted in BET specific surface area of 1472 m^2/g and a pore volume of 1.69 cm^3/g, as mentioned in Table 1.

Pore size distributions obtained by BJH model applied to the desorption brand (see Fig. 2 B and C) are in the 2–400 nm range. Asparagus:$ZnCl_2$ (1:2) shows a narrower distribution peaked around 4 nm, while Asparagus:$ZnCl_2$ (1:3) has a broader distribution with a higher fraction of large pores. These results are supported by the NL-DFT pore size distributions, reported in Fig. S1†. Both materials show strong evidence of hierarchical porous structure with a sizeable micro- and meso-porosity, thanks to the chemical activation by $ZnCl_2$ followed by the physical activation with CO_2. These distributions showed that the specimen Asparagus:$ZnCl_2$ (1:3) contains slightly larger pores than Asparagus:$ZnCl_2$ (1:2). The STSA and the micropore surface area for the two samples are reported in Table 1. The detailed discussion about STSA is reported in the supporting information. Since Asparagus:$ZnCl_2$ (1:2) has a higher BET surface area and higher microporosity, the rest of the studies have been performed on Asparagus:$ZnCl_2$ (1:2) activated carbon powder.

3.1.2. Scanning electron microscopy

SEM images of optimized AC powder are shown in Fig. 3 (A-D) at three different magnifications (from x100 to x5000). The material appeared in form of flakes and grains with typical size of hundreds of micrometres. Some grains still preserved the tubular architecture, reminiscent of the presence of sieve vascular bundles in the starting material, even after the carbonisation. The presence of small granules in ACs helps to expose most of the carbon material to the outer atmosphere [25]. EDS analysis highlighted that most of the material is carbon (approx. 90 wt%), with traces of heteroatoms, such as S and P. Data have been reported in the supplementary information.

Fig. 3 (E) shows the X-ray pattern of the optimized AC powder, which shows two distinct broad peaks at 2θ ~23° and at 2θ ~43°, a disordered structure bearing similarities with graphite, in which peaks are typically found at 2θ ~26° and at 2θ ~42°, corresponding to (002) and (100) planes, respectively. The broad and distinct peaks show that the activated carbon powder, which is produced by the carbonisation process at about 800 °C, is primarily amorphous and has less developed intra-graphitic layers (i.e., a lower fraction of crystalline graphitic domains). Under these circumstances, it's possible that the graphitization either doesn't start or doesn't finish [60]. The majority of the carbonized structure is comprised of bent aromatic units that are translated and rotated in relation to one another [61] or nano-sheets. Therefore, the (002) peak broadens in the AC structure as opposed to being narrow and well-defined in pure graphite due to the disorganised arrangement [61–64]. Rotation of the planes relative to one another and an increase in the interplanar distance are the main factors influencing the position and intensity of the (100) peak [65]. The peak in this case is at a comparatively smaller angle (43.7°) than in ordinary pure graphite (44.3°), indicating that the curvature and rotation about the perpendicular axis lead to the arrangement of the aromatic planes towards a slightly larger spacing [65].

The structural properties of the optimized AC powder have been investigated by using micro-Raman spectroscopy, as shown in Fig. 4.

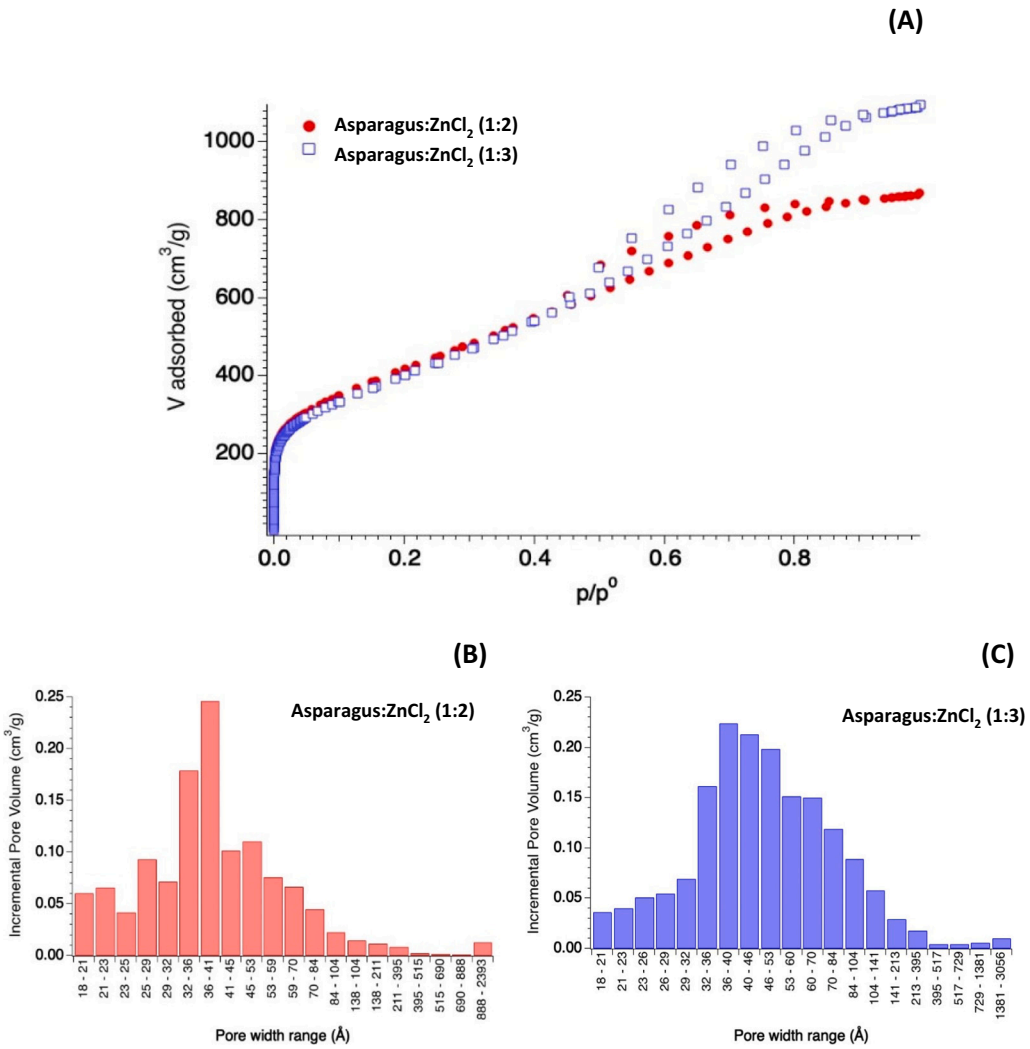

Fig. 2. (A) N_2- adsorption-desorption isotherms, (B and C) Pore size distributions obtained by BJH method.

Table 1
Surface area and pore volume values.

Sample	Biomass: $ZnCl_2$	BET surface area (m^2/g)	Pore volume (cm^3/g)	STSA (m^2/g)	Micropore surface area* (m^2/g)
Asparagus: $ZnCl_2$ (1:2)	1:2	1516	1.24	1443	73
Asparagus: $ZnCl_2$ (1:3)	1:3	1471	1.69	1518	47

* By calculating the difference between the total and external surface areas, the micropore surface area was calculated: $S_{micropore} = S_{BET}$-STSA.

The carbon material shows the expected spectrum of amorphous carbon, with two major bands at ~1360 cm^{-1} and ~ 1600 cm^{-1}, known as D-band and G-band respectively (shown by red lines). The G-band corresponds to in-plane vibrations of sp^2 hybridized carbon [66,67], whereas the D-band is related to the presence of defects and disorder in the imperfect crystalline structure (e.g. carbon vacancies, sp^3 hybridized carbon) [68]. Other contributions in the spectrum were highlighted by the band deconvolution and the results are reported in Fig. S2†.

The in-plane average crystallite size (sometimes referred to as L_a) may be related to the ratio of the integrated areas of the D-band and G-band (I_D/I_G) [69]. For the AC powder, a value of ~1.3 is compatible with a nanometric size of the crystallites.

3.2. Electrochemical properties of GPE

The GPE film has superior mechanical and electrochemical stabilities, and its ionic conductivity (σ) at room temperature is approximately 10^{-3} S cm^{-1}. The ionic conductivity of the GPE has a major impact on the supercapacitors performance, specifically on the internal resistance and therefore the power density of the device. GPE used in this article comprising of 1 M LiTFSI in (ionic liquid) BMPTFSI, immobilized in PVdF-HFP, is a semi-transparent, flexible, free-standing thick film of thickness 0.35–0.54 mm, as shown in Fig. 5 (A). Multiple mechanical stresses, including twisting, bending and stretching, have been applied to the film. This indicates that the GPE films can be easily deformed, twisted, stretched, and bent into a spiral shape Fig. 5 (B-E) which can be very useful in developing flexible supercapacitors [21,46]. Additionally, it has been shown that the GPE can return to its initial shape very quickly following the elimination of external stresses [46]. At room temperature (~ 27 °C), the calculated ionic conductivity of GPE film is found to be ~6.3×10^{-3} S cm^{-1}, which was calculated by using the equation; $\sigma = l/(R \times A)$, where l and R are the thickness and bulk resistance of the GPE respectively, while A is the area of the GPE.

Another significant parameter directly associated with the performance of EDLCs is the ESW of electrolytes [46]. Electrolytes having high

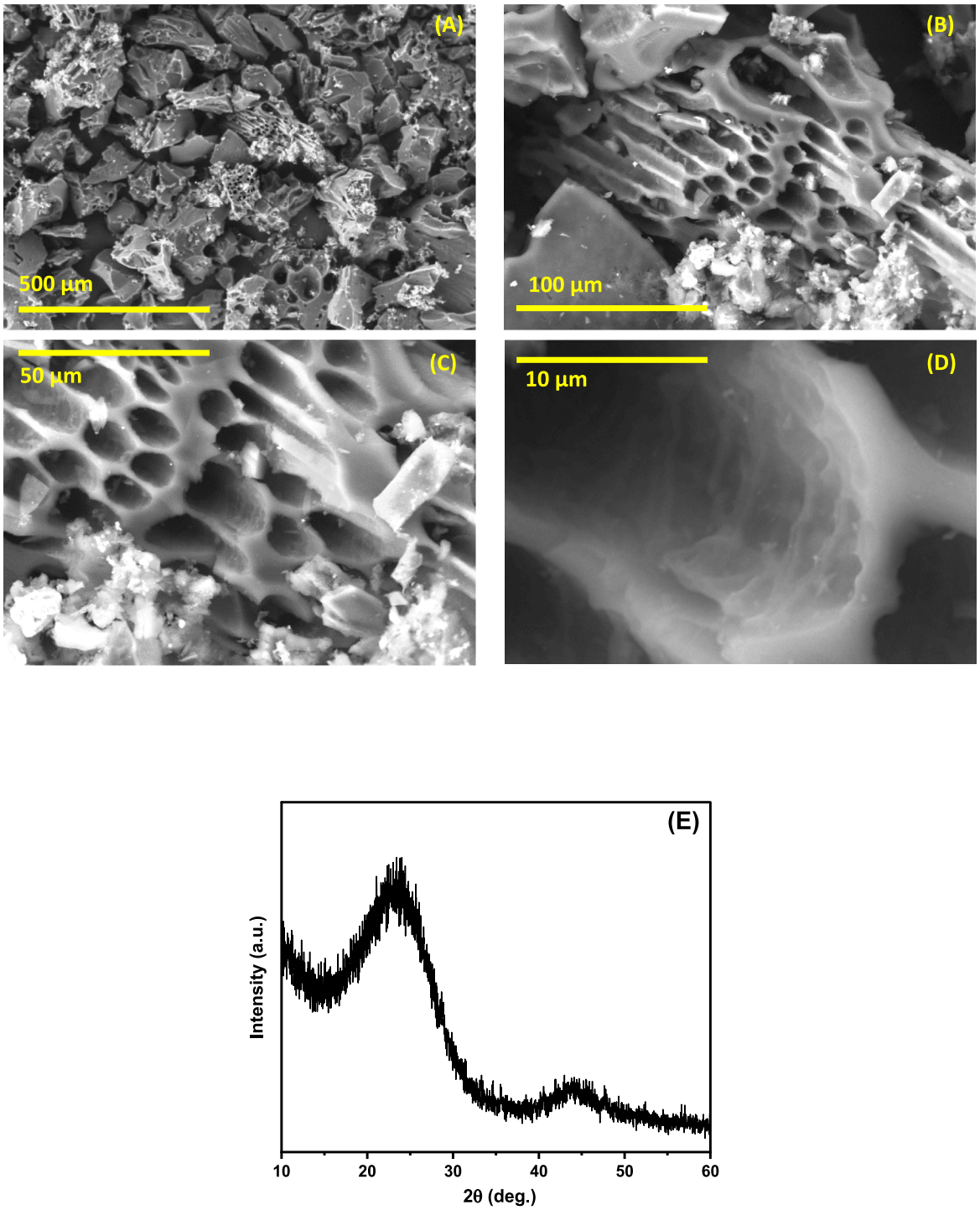

Fig. 3. SEM images of optimized AC powder at different magnifications (A) x100 (B) x500 (C) x1000 (D) x5000 (E) Powder X-ray diffraction pattern of AC powder.

ESW help devices attain higher operating voltage windows, and consequently higher specific energy [46]. The ESW of the GPE was measured with LSV in two-electrode configuration. Fig. 5(F) displays the LSV pattern at a scan rate of 10 mVs^{-1}, from −2 V to 3.2 V vs Ag/Ag^{+} of the GPE. The GPE exhibit high ESW of ~4.5 V, which is a quite wide working voltage stability window for EDLC applications. The GPE is stable up to −1.5 V and 3 V versus Ag/Ag^{+} in the cathodic and anodic range, respectively. This wide stability range indicates that the GPE can be used not only in supercapacitors, but also and in other electrochemical energy storage devices [21].

3.3. Performance studies of supercapacitors/EDLCs

3.3.1. Electrochemical impedance spectroscopy (EIS) studies

The supercapacitors/EDLCs comprised of both GPE and liquid electrolytes have been characterized with EIS analysis (Cell-1 and Cell-2 respectively) in the frequency range from 10 mHz to 100 kHz. EIS analysis provides useful information about charge-transfer resistance, bulk resistance, diffusion of ions at electrode/electrolyte interface and capacitive behaviour of the EDLC cells. EIS (Nyquist) graphs for Cells 1 and 2 (i.e., Z' vs Z" plot with varied frequencies) are displayed in Fig. 6 (A-B), respectively. The low frequency section of the impedance spectra

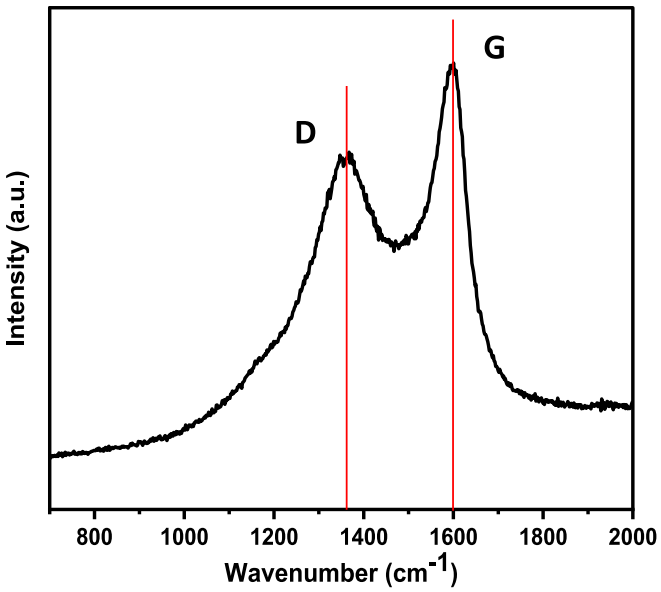

Fig. 4. Raman spectrum of optimized AC powder.

of both cells exhibits a rapidly increasing straight line character, indicating the capacitive behaviour of the cells. The zoomed plots of EIS spectra in high/mid frequency region show different features (combination of semi-circular and curved nature) for the EDLCs, as shown in the insets of Fig. 6 (A-B), which is the union of electric double layer capacitance and faradic charge-transfer resistance in parallel, representing the bulk resistance in a series [21]. As shown by arrows in the insets of Fig. 6 (A-B) and stated in Table 2, the values of bulk and charge-transfer resistance, R_b and R_{ct}, for both cells are computed from the intercepts of the semicircular arcs with the Z'-axis for Z" = 0. The bulk resistance (R_b) can be attributed to a combination of electrode and electrolyte resistances, while charge-transfer resistance (R_{ct}) generally does not appear in carbon electrodes-based supercapacitors because of the electrostatic charge storage mechanism and no redox (Faradaic) reactions are expected at the electrode/electrolyte interfaces [70]. However, in the cells under consideration, a well-defined semicircle can be observed, and hence a finite value of R_{ct} can be observed. This effect may be caused by redox interactions between electrolyte ions and the functional groups at the porous carbon surface, such as -OH, -C=O, -COOH [70].

Both the cells have comparable resistive values including charge-transfer resistance (R_{ct}) which implies that the electrode/electrolyte interface exhibits appropriate development of an electric double layer. A significant difference in the bulk resistance (R_b) value between the two cells can be explained as easy access of liquid electrolyte ions to the pores of the electrode material, whereas in the case of GPE the accessibility of the AC pores is hindered. Further comparison shows that both cells have comparable values of specific capacitance (C_{sp}), calculated from the formula: $C_{sp} = 2/(2\pi f \times m \times |Z"|)$, where (m) is the mass of the active material employed in the single electrode, (f) is the frequency (10 mHz in this case), and ($|Z"|$) is the magnitude of the imaginary component of the impedance [46]. The comparative values of C_{sp} for the supercapacitors, including the resistive parameters (R_b, R_{ct}), have been listed in Table 2. The actual values of specific capacitance and energy densities were evaluated from the GCD measurements by obtaining the equivalent series resistance (ESR) from the discharge curves.

Further analysis reveals that the GPE-based cell (Cell-1) has a broad linear region of EIS pattern observed in the mid-frequency band between the semi-circular arc and the sharply increasing, capacitive-typical straight line, as shown in the inset of Fig. 6 (A). In the case of the liquid electrolyte, this region is almost negligible as compared to GPE based cell as shown in the inset of Fig. 6 (B). The electrolyte resistance in the porous interiors of the carbon electrodes, which is known as internal resistance, has an impact on these narrow or wider regions [70]. Warburg impedance, which is primarily associated with the regulated passage of electrolyte ions through the pores of the carbon material, is represented by the sharply increasing curve in this area [2,54,70,71].

Additionally, to better understand the electrochemical processes in the EDLCs across a variety of frequency ranges, the EIS data (for each cell i.e., Cell-1, and Cell-2) has been fitted with a common equivalent circuit in the mid to high frequency area by simulating the necessary circuit components, as shown in the insets of Fig. 6 (A-B). Different circuit elements, such as the constant phase element (CPE), Warburg elements (W and Wo1), and resistive values (R_1 and R_2), are employed to fit the curves to assess the nature of the Nyquist behaviour; fitting parameters are listed in Table S1†. The fitted parameters R_1 and R_2 of the circuit elements of both cells are consistent with the obtained experimental EIS curves values bulk resistance (R_b) and charge transfer values (R_{ct}), respectively listed in Table 2. The close values of fitted parameters to the experimental values show the goodness of fit of the equivalent circuit model. Here, the constant phase element (CPE), a circuit element representing a double layer in the form of an imperfect capacitor, is represented by $Z_{CPE}(\omega) = Q^{-1} \times (j\omega)^{-n}$, where Q represents the capacitance for $n = 1$ [2,46,70]. The finite value of Warburg (W) for each cell represents the finite diffusion of electrolyte ions through the carbon electrodes pores. The Warburg open element (W_{o1}) represents the impedance of finite-length diffusion which is denoted by equation [46,72];

$$Z_{W_{o1}} = \frac{W_{or}}{\sqrt{j\omega}} \coth\left(W_{oc} \times \sqrt{j\omega}\right) \quad (1)$$

where, W_{or} represents the Warburg coefficient, $W_{oc} = d/D^{0.5}$ (d = Nernst diffusion layer thickness and D = diffusion coefficient of the electroactive species), and ω is the frequency of the applied signal [46,72].

Fig. 6 (C) shows the real and imaginary capacitances (C′ and C“) variation with respect to the frequency change (10 mHz to 100 kHz) for Cell-1, which helps understand the ion diffusion mechanism in the carbon electrodes pores with respect to the frequency variation. The C' and C" versus frequency plots for Cell-2 are shown in the inset of Fig. 6 (C). The values of C′ and C″, related to the real and imaginary impedances (Z′ and Z") which are obtained from the Taberna approach, are expressed here in terms of following equations [21,73];

$$C'(\omega) = \frac{-Z''(\omega)}{\omega|Z(\omega)|^2} \quad (2)$$

$$C''(\omega) = \frac{Z'(\omega)}{\omega|Z(\omega)|^2} \quad (3)$$

Both the supercapacitors (Cells 1 and 2) show rapidly decreasing behaviour of real capacitance (C′) in low frequency region below ~1 Hz, with values comparable to the capacitance values obtained from galvanostatic discharge tests, discussed later. Additionally, each cell exhibits a nearly zero slope of real capacitance (C′) in the 10–10^5 Hz high frequency band, confirming the supercapacitors comparatively low capacitive contribution to the high frequency area. Furthermore, below 10 Hz, by decreasing the frequency the C′ values rapidly increase towards a maximum in the capacitance. The variation of the imaginary capacitance (C″) versus frequency shows a peak type of behaviour in the frequency domain 0.01–10^2 Hz and after that it tends to zero, which indicates that the supercapacitors (Cell-1 and Cell-2) display a relaxation-type nature [2,70]. As frequency increases, the observed peaks in the C" versus frequency graphs indicate the general behaviour of porous carbon electrode-based supercapacitors, which is the transition from the capacitive to the resistive domain [46,74].

The phase angle variation for EDLC cells (Cells 1 and 2) vs frequency is displayed in Fig. 6(D). The horizontal line in Fig. 6 (D) represents the

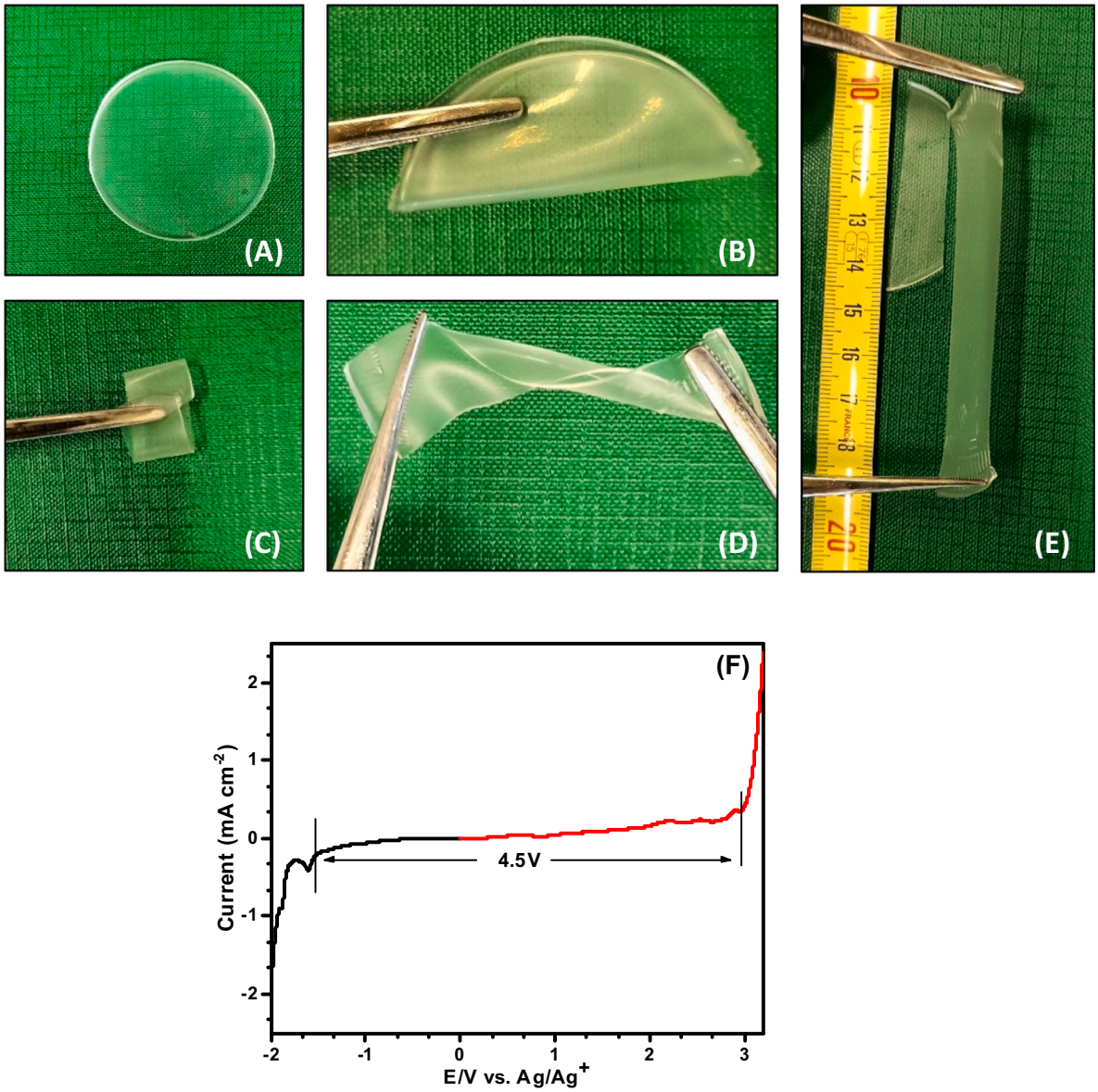

Fig. 5. (A-E) Images of GPE films during bending, twisting, and stretching tests, and (F) LSV measurement of the GPE film for the evaluation of ESW.

phase angle of 90° for an ideal capacitor over the whole frequency range. In this particular case, the EDLC cells Cell-1 and Cell-2 exhibit lower frequency range phase angles of 85.2° and 88.3°, respectively. This highlights the lower frequency range-limited capacitance behaviour of EDLC cells, which has been addressed before in the Nyquist plot Fig. 6 (A-B).

In order to obtain additional insight into the rate performance of the EDLC cells (Cell-1 and Cell-2), real and imaginary impedance values (Z' and Z") have also been recorded and plotted against frequency (Bode plots), as shown in Fig. 6 (E). The characteristic frequency (f_0) values for Cell-1 and Cell-2 have been determined from the Z', Z" Bode plots to be 0.25 Hz and 0.49 Hz, respectively (indicated in Fig. 6 (E) with arrows). The characteristic frequency, also referred as response frequency, is the value of the frequency at which the real and imaginary impedance (Z' and Z") intersect each other, and at which the phase difference between the Z' and Z" is ~45°. The pulse-power, or "figure of merit," of supercapacitors has been used to assess the rate performance of the cells [75]. The expression $P_0 = E_0 / \tau_0$, where E_0 is specific energy evaluated at f_0 and τ_0 is response time, which is the reciprocal of the response frequency ($\tau_0 = 1 / f_0$), has been used to evaluate the pulse power at the characteristic frequency f_0. Energy and pulse power densities have been listed in Table 2 for the supercapacitors. Specific energy has been evaluated from the equation:

$$E_0 = \frac{1}{4m} \times C_0 V^2 \quad (4)$$

where m is the active mass employed in the single electrode, V is the rated voltage of the cells (V = 2.3 V for GPE-based cell, and C_0 is the capacitance of the single cell at f_0) [54]. Further comparison shows that Cell-1 shows higher pulse power density value in contrast with the Cell-2 (Table 2). This indicates that GPE based cell has higher rate capability as compared to liquid electrolyte-based cell. The explanation for the GPE-based cell for having higher rate capability is possible that charge-transfer via electrolyte ions of quasi-solids, such as GPE, is limited to the shallower extent of the electrode interior pores, whereas liquid electrolyte ions have deeper access to bulk electrodes [54].

3.3.2. *Cyclic voltammetry*

Cyclic voltammetry in a two-electrode system has been used to assess the electrochemical performance of the EDLC cells (Cell-1 and 2). As

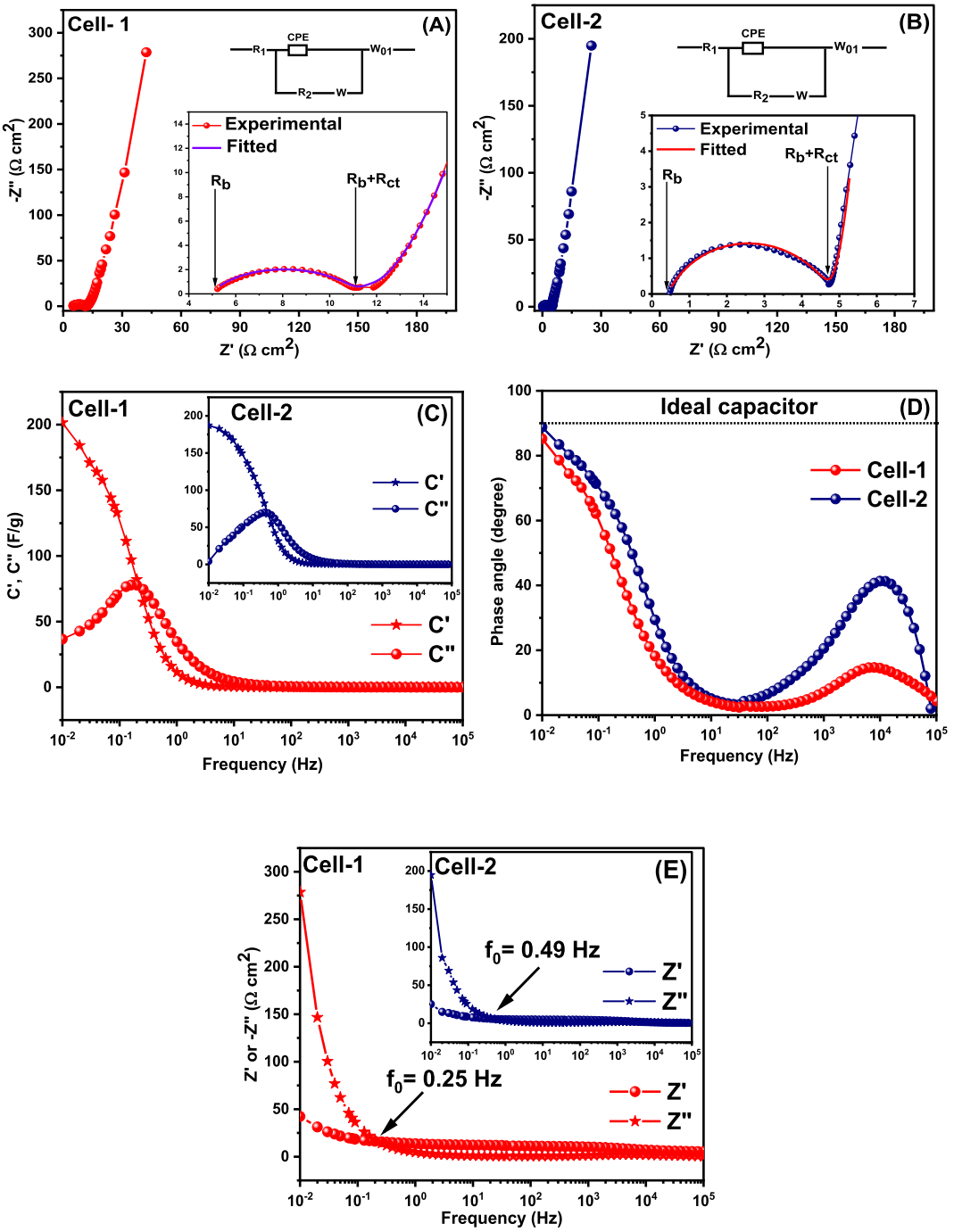

Fig. 6. (A-B) EIS (Nyquist) plots of EDLC cells in the frequency range from 10 mHz to 100 kHz (the corresponding circuit and extended EIS plot in the high frequency region are displayed in the corresponding inset), (C) real and imaginary capacitance (C′ and C″) versus frequency of both cells, (D) phase angle as a function of frequency for both the cells, (E) real and imaginary impedance compared to the frequency graphs (Bode plots) of the cells.

Table 2
Electrical parameters of supercapacitors calculated from EIS studies.

EDLCs	R_b / Ω cm^2	R_{ct} / Ω cm^2	C_{sp} / F g^{-1}	E_0 / Wh kg^{-1}	P_0 / kW kg^{-1}
Cell-1	5.1 ± 1.1	6.7 ± 1.3	123.3 ± 4	16.1 ± 1.1	14.5 ± 2.2
Cell-2	0.5 ± 0.8	4.2 ± 0.9	136 ± 3	4.1 ± 0.9	7.2 ± 1.8

shown in Fig. 7 (A-B), the CV curves for various voltage ranges have been acquired at a constant scan rate of 10 mV s^{-1} to evaluate the appropriate voltage window of the EDLC cells. The CV curves substantially deviate from their regular box-like rectangular nature beyond 2.3 V for Cell-1, while the deviation can be observed beyond 1.2 V for Cell-2 Fig. 7 (A-B). This suggests an ideal voltage range of 0 to 2.3 V for Cell-1 and 0 to 1.2 V for Cell-2. Although a slight current increase can be observed at 1.2 V, the choice of the 1.2 V voltage window is supported by the galvanostatic charge-discharge (GCD) results, which will be discussed later. Therefore, in subsequent experiments, both cells have been electrochemically tested for the optimal window of 0–2.3 V for the GPE-based cell and 0–1.2 V for the liquid electrolyte-based cell. These ideal voltage ranges for both cells have also been verified by GCD investigations, which will be addressed later. The lower potential window

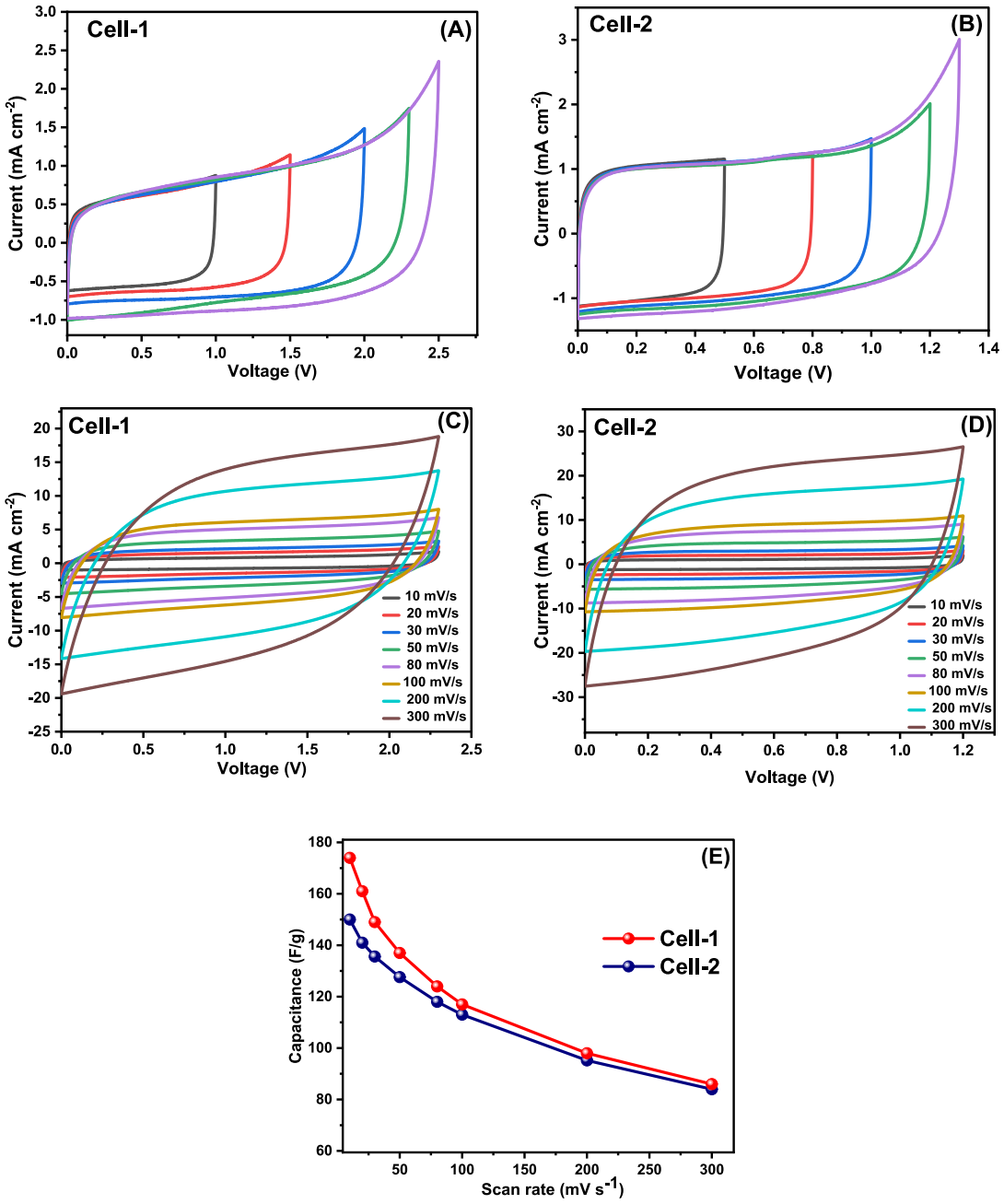

Fig. 7. (A-B) CV pattern of EDLC cells Cell-1 and Cell-2, for varying potential at a scan rate 10 mV s^{-1}, (C—D) CV responses of Cell-1 and Cell-2 recorded at different scan rates from 10 to 300 mV s^{-1}, (E) shows the EDLC cells specific capacitances scan rate dependence.

of Cell-2 as compared to Cell-1 is due to the water electrolysis reaction since Cell-2 is fabricated with aqueous electrolyte i.e. 7 M KOH. At higher potential, water molecules can undergo electrolysis that leads to the production of oxygen and hydrogen gas which limits the electrochemical stability of the SC.

As shown in Fig. 7(C—D), the scan rate dependent CV curves have been acquired for both Cell-1 and Cell-2 in order to assess the rate capability of the EDLC cells up to the maximum scan rate of 300 mV s^{-1}. Up to 200 mV s^{-1}, the voltammograms of the EDLC cells (Cell-1 and Cell-2) exhibit an essentially rectangular shape; nevertheless, there is a noticeable variation in shape after that. This points out that the liquid electrolyte-based and GPE-based cells have a moderate rate capability. The well-connected, hierarchical porous nature of the activated carbon powder produced from asparagus waste, which enables easy electrolyte ion switching through the pores, contributes to the improved rate capability of the capacitor interfaces between the activated carbon electrode and electrolyte [60].

The specific capacitance variation for the EDLC cells (Cell-1 and Cell-2) as a function of scan rate is illustrated in Fig. 7(E). The values of specific capacitance (C_{sp}) have been calculated by using the equation:

$$C_{sp} = \frac{2 \times j}{s \times m} \tag{5}$$

where m is the mass on a single electrode (per cm^2) in the cell, s is the scan rate (mV s^{-1}), and j is the current density in the centre of the voltage range. Comparing Cell-1 to Cell-2, Cell-1 exhibits greater capacitance values and maintains superior performance throughout all scan-rates. The C_{sp} values in both Cell-1 and Cell-2 of the EDLC exhibit a sharp initial decline, which is followed by a steadier decline in values at higher scan rates. The following explanation is proposed. Reduced scan

rates cause the ions to adsorb at electrode-electrolyte interfaces more slowly and consequently all of the ions to fully diffuse inside the pores, increasing specific capacitance values and charge storage [21]. On the other hand, at higher scan rates the diffusion layer may have formed over a shorter distance [21]. The decrease in specific capacitance is likely due to the inability of the ions to reach the deeper region of the carbon materials pores [21].

3.3.3. Galvanostatic charge-discharge

Cells-1 and 2 have undergone GCD experiments to assess the specific discharge capacitance (C_{sp}) at various current densities, power and specific energy, rate performance, and cyclic efficiency. First, to optimize the maximum voltage window, the EDLCs have been subjected to varying applied voltage ranges as mentioned in Fig. 8 (A-B). Clearly, it can be seen that Cell-1 shows almost triangular shape of GCD curve in the potential window 0–2.3 V while Cell-2 has almost linear charge-discharge GCD profile in the voltage range 0–1.2 V after that, the curves significantly depart from their linear characteristics. Also, the coulombic efficiency of the cells reduces significantly from ~92–94 % to ~85–88 % beyond the optimum voltage window range. The charge storage in the EDLC cells is mostly due to a suitable electric double layer at the electrode/electrolyte interfaces, as demonstrated by the linear charge-discharge pattern in GCD curves up to a particular voltage [21]. Thus, in additional GCD investigations of EDLCs, Cell-1 and Cell-2 have been charged-discharged in the potential range of 0 to 2.3 V and 0 to 1.2 V, respectively. This optimal voltage window have been confirmed from CV measurements, especially for Cell-1. For Cell-2, GCD analysis demonstrated that the coulombic efficiency maintained approximately 94 % up to 1.2 V. Beyond this threshold, efficiency starts to decline below 90 %. Therefore, 1.2 V was chosen as the top limit to ensure high efficiency and excellent performance of the supercapacitor.

Using the following formula, the equivalent series resistance (ESR) values of the EDLC cells have been calculated from the abrupt voltage drop upon current reversal, or when the cell transitions from a charging to a discharging profile [60,76]:

$$\mathrm{ESR} = \frac{\Delta V}{2\,|j|} \tag{6}$$

where j is the steady current and ΔV is the abrupt voltage drop that occurs when the current reverses polarity at the start of the discharge step [60]. The following formula has been used to determine the specific discharge capacitance (C_{sp}) due to the fact that the discharge curve is not completely linear [70]:

$$C_{sp} = \frac{4\,\mathrm{j}\int \mathrm{V}\,\mathrm{dt}}{\mathrm{m} \times V^2\big|_{V_i}^{V_f}} \tag{7}$$

where $\int \mathrm{V}\,\mathrm{dt}$ is the area under the discharge curve; V is the maximum operating voltage; j is the current density; m is the mass of active material on a single electrode (excluding the mass of the binder and

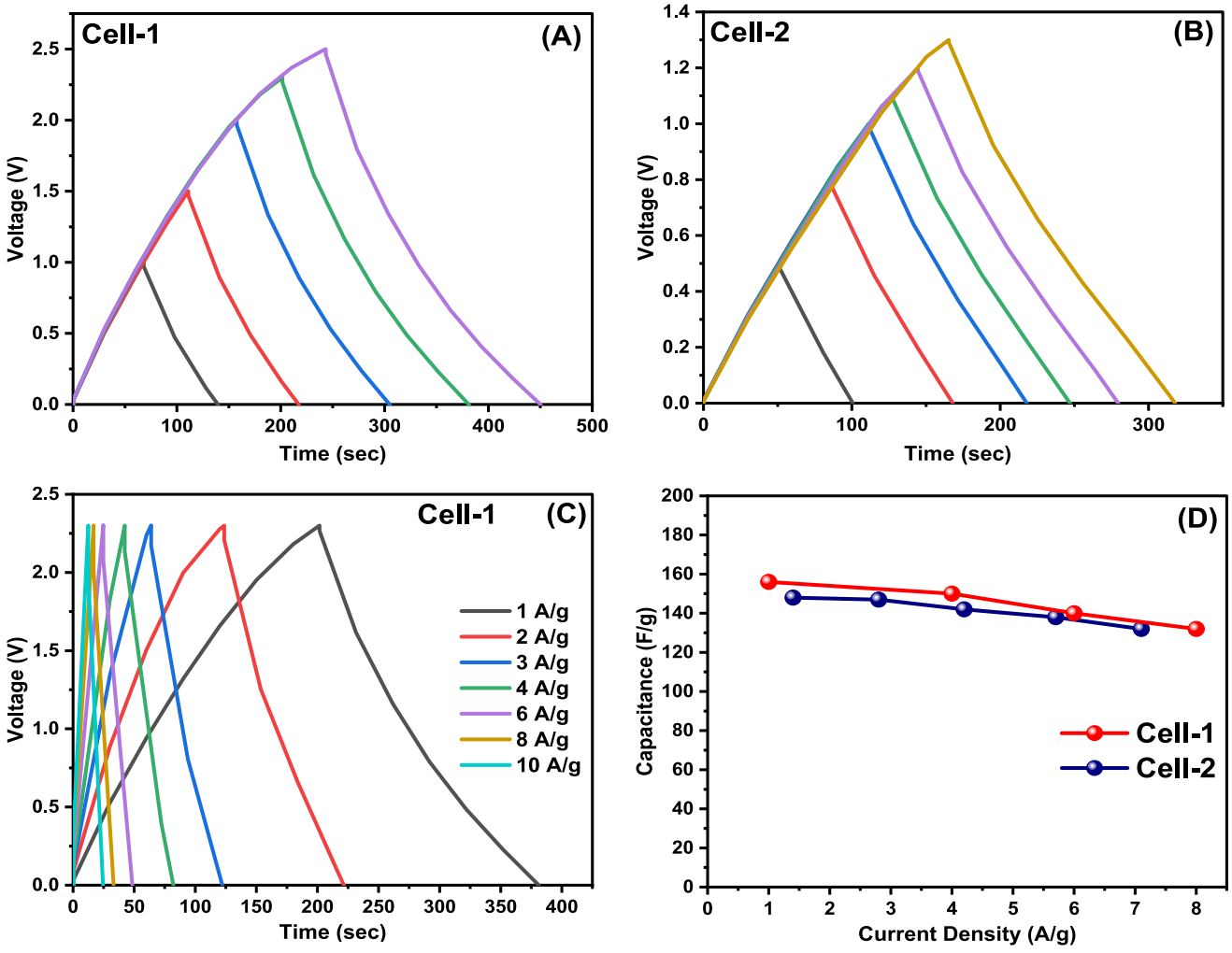

Fig. 8. (A-B) GCD curves of supercapacitors Cells-1 and Cell-2 for a range of voltages at a current density of 1 mA cm^{-2} (or 1 A/g and 0.7 A/g for Cell-1 and Cell-2, respectively) (C) Cell-1 GCD curve at various current densities, and (D) variation in specific capacitance (C_{sp}) versus applied current density for supercapacitors.

conductive additive); and V_i and V_f are the initial and final voltage on the GCD curves [70]. ESR and C_{sp} for each of the cells are shown in Table 3.

Both the cells show comparable values of ESR and specific discharge capacitance (C_{sp}), as mentioned in Table 3, indicating that AC powder has sufficiently higher content of microporosity and a higher specific surface area. Along with the microporosity, the carbon powder has mesoporous contribution which acts as a transport route for faster ion mobility. Cell-1 is characterized by a substantially higher capacitance as compared to Cell-2, which is expected, as the ions in GPE has restricted accessibility to deeper region of the pores of the carbon material, while liquid electrolyte ions have access to deeper pores in the AC. Hence, the lower capacitance in Cell-2 can be explained with a partial blocking of the inner pores by a fraction of the ions in the liquid electrolyte, so they cannot exploit the entire specific surface area present in the AC to the deeper extent.

The GCD curves of the Cell-1 at various current densities (ranging from 1 to 10 A g^{-1}) in the voltage range of 0 to 2.3 V are depicted in Fig. 8(C). The graph of the GCD curve shows that even at a high current density of 10 A g^{-1}, the ideal triangular shape has been retained, demonstrating that, up to a high current density of 10 A g^{-1}, the charge-discharge mechanism is steady. The specific discharge capacitance (C_{sp}) for both cells, which have also been assessed at various current densities, are shown in Fig. 8(D). This can be directly related to the EDLC cells rate performance. As the current density for both Cell-1 and Cell-2 increases, it can be observed that the specific discharge capacitance (C_{sp}) decreases gradually. This is because the ions at the electrode-electrolyte interfaces are forced to move more rapidly, causing a faster rate of adsorption-desorption at the interface. Hence, ions cannot exploit all the accessible surface area at higher current densities in comparison to the slower current densities. The C_{sp} slowly decreases at increasing scan rates for values greater than ~6 A g^{-1}, which is explained by the increased contribution of carbon material mesopores for quicker ion movements. Across the whole current density range, nearly parallel curves are seen for both cells, suggesting that the GPE-based cell performs well at a higher rate. Several more reasons could justify a higher capacitance in Cell-1, such as uniform and intimate contact with electrode materials, increasing ion accessibility and effective surface area for charge storage. Additionally, GPEs maintain mechanical stability and prevent electrolyte leakage or evaporation, ensuring consistent performance and sustained high capacitance over long cycles.

The maximum and effective power densities, as well as specific discharge energy/specific energy, have all been computed in relation to the EDLC cells. The specific energy (E_{sp}) of the supercapacitors have been calculated from the non-linear discharge curve, using the following expression [70,77]:

$$E_{sp} = \frac{j \times \int V\,dt}{2m} \tag{8}$$

where $\int V\,dt$ is the area under the discharge curve, V is the highest voltage of charge-discharge, *j* is the constant current, and m is the mass of the active carbon in a single electrode [25,70]. Additionally, the following formulae have been used to calculate the effective power density (P_{eff}) and maximum power density (P_{max}) of both cells [25,70]:

$$P_{max} = \frac{V^2}{8m \times ESR} \tag{9}$$

Table 3
Parameters assessed using EDLC cells GCD analysis at a constant current density of 1 mA cm^{-2}.

EDLCs	ESR / Ω cm^2	C_{sp} / F g^{-1}	E_{sp} / Wh kg^{-1}	P_{eff} / kW kg^{-1}
Cell-1	16–20	151–160	28–31	0.54–0.56
Cell-2	4–7	141–153	6–7	0.18–0.19

$$P_{eff} = \frac{E_{sp}}{t_{dis}} \tag{10}$$

where, ESR is the equivalent series resistance and t_{dis} is the discharge time of the EDLC cells [70,77]. The parameters namely P_{eff} and E_{sp} have been assessed at a typical current 1 mA cm^{-2} for both the cells and listed in the Table 3. The Cell-1 exhibits higher energy density by ~4 times as compared to the Cell-2, which confirms the advantage of gel polymer electrolyte over liquid electrolyte since GPE based cell has approximately ~2 times larger voltage window in comparison to the liquid electrolyte-based cell.

Further, the effective power (P_{eff}) of Cell-1 is higher than Cell-2, mentioned in Table 3. As was previously indicated, the GPE-based cell has a greater rate capability and greater effective power because its interface allows faster ion switching motions than the liquid electrolyte-based cell [54].

The obtained key parameters such as specific capacitance, specific power, and specific energy of the current study have been compared with those reported for recently published supercapacitors that utilize various biomass-derived carbon electrodes, as summarized in Table 4. Furthermore, comparison with many other documented systems reveals that current EDLCs made with carbon electrodes produced from asparagus waste exhibit equivalent or even greater values of specific capacitance, power, and energy Table 4 [78–92].

Fig. 9(A) displays Ragone plots for both cells, showing the specific energy (E_{sp}) against effective power density (P_{eff}). It has been found that both cells show similar nature of Ragone plots of other EDLCs/supercapacitors reported in literature [46]. In particular, both the cells show similar behaviour, with an increase in the effective power at cost of decrease in the specific energy values. In comparison to Cell-2, Cell-1 performs better thanks to higher specific energy values for each effective power value Fig. 9(A). The exceptional quality of an EDLC is demonstrated by the specific power increase of 11 times, from ~0.56 to ~6.1 kW kg^{-1}, and a specific energy variation of ~29 to ~23 Wh kg^{-1}. A LED with a power output of about 38–50 mW was used to rate the device as a power source. To achieve this, as illustrated in Fig. 9(B), three optimized GPE-AC cells were connected in series, completely charged, and connected to the red LED, which flashed for about 90 s before fading. This demonstrates the cells effective capacity for energy storage.

A lengthy cyclic test, with respect to specific discharge capacitance (C_{sp}) and coulombic efficiency η (%) as a function of number of charge-discharge cycles Fig. 9(C), was performed on both Cell-1 and Cell-2. The coulombic efficiency η (%) has been assessed from the following equation:

$$\eta = \frac{t_D}{t_C} \times 100\% \tag{11}$$

where, t_C and t_D are the constant current discharging and charging time, respectively. The cycling performances for long charge-discharge cycles have been evaluated between 0 and 2 V and 0 to 1.2 V for Cell-1 and Cell-2, respectively at 1 mA cm^{-2} (1 A/g and 0.7 A/g for Cell-1 and Cell-2, respectively) to keep their GCD curve in close to ideal conditions [46]. It is clear from Fig. 9(C) that Cells 1 and 2 exhibit a rapid fading in specific capacitance of approximately 16 % and 18 %, respectively, for the first approximately 1000 cycles. After that, a progressive fading is observed up to 10,000 cycles. When it comes to discharge capacitance as a function of cycle number, Cell-1 performs better here as well. The rapid fading observed in both cells during the first ~1000 cycles may be attributed to irreversible interactions with the surface functionalities deposited on carbon electrodes and the development of a passivation layer at the interfaces between the electrode and electrolyte [21,46]. Once the numerous electrochemical reactions balance with one another, the cells stabilise after around ~1000 cycles, and the capacitance fading is quite slow [21]. This slow fading also indicates that few small pores/micropores in the carbon material are getting slowly blocked as the

Table 4
Comparing carbon electrodes for EDLCs made from biomass.

Biomass Precursor	Pre-activation treatment	Activating agents	Activation temperature/°C	Surface area /(m^2/g)	Electrolyte	Specific capacitance (Fg^{-1})	Specific energy ($Whkg^{-1}$)	Specific power ($kWkg^{-1}$)	Ref.
Wheat Straw	Pre-Carbonisation	KOH	800	1486	PVA/KOH solid electrolyte	294 at 1 A g^{-1}	14	0.44	[78]
Corn Stover	Pyrolysis	KOH	800	2441	1 M H_2SO_4	398 at 0.5 A g^{-1}	5.01	0.1	[79]
Cottonseed meal	Hydrothermal treatment	K_2CO_3	800	2361	6 M KOH	71.8 at 0.5 A g^{-1}	34.4	0.225	[80]
Bamboo	NA	K_2CO_3	800	1802	–	–	–	–	[81]
Banana stem fibers	NA	$ZnCl_2$	900	788.09	1 M H_2SO_4	179	6.19	0.044	[82]
Onion Husk	NA	K_2CO_3	800	2571	1 M $TEABF_4$/ AC	188 at 1 A g^{-1}	35.4–47.6	0.675–20.25	[84]
Peanut shell	NA	$ZnCl_2$	550	1549	1 M H_2SO_4	333 at 0.5 A g^{-1}	8.5–4.6	0.1–6.56	[83]
Rice Bran	Pyrolysis	KOH	850	2475	6 M KOH	323 at 0.1 A g^{-1}	70	1.223	[85]
Pinecone	NA	$ZnCl_2$	800	1781	GPE (PVdFHFP/ SN/EMITF/ LITFSI)	255 at 1 mA cm^{-2}	20	0.055	[86]
Pollen cone	Pre-carbonized	KOH	800	2314	GPE (PVdFHFP/ EMITFSI)	146 at 0.5 A g^{-1}	21	0.19	[54]
Rice straw	Pre-carbonized	KOH	800–900	2651	6 M KOH, EMITFSI	324 at 0.5 A g^{-1}	48.9	0.75	[88]
Tabacco waste	Hydrothermal treatment	KOH	800	1875.5	6 M KOH	356.4 at 0.5 A g^{-1}	10.4	0.3	[89]
Corncob	NA	Steam	850	1210	6 M KOH	120 at 1 A g^{-1}	5.3	8.276	[90]
Coffee bean	NA	H_3PO_4	800	742	1 M H_2SO_4	160 at 1 A g^{-1}	15	0.075	[91]
Cotton stalk	NA	H_3PO_4	800	1481	1 M $TEABF_4$/ AN	114 at 0.5 A g^{-1}	–	–	[92]
Asparagus waste	NA	$ZnCl_2$	800	1516	GPE (LiTFSI/ BMPTFSI)	153 at 1 A g^{-1}	31	0.56	This work

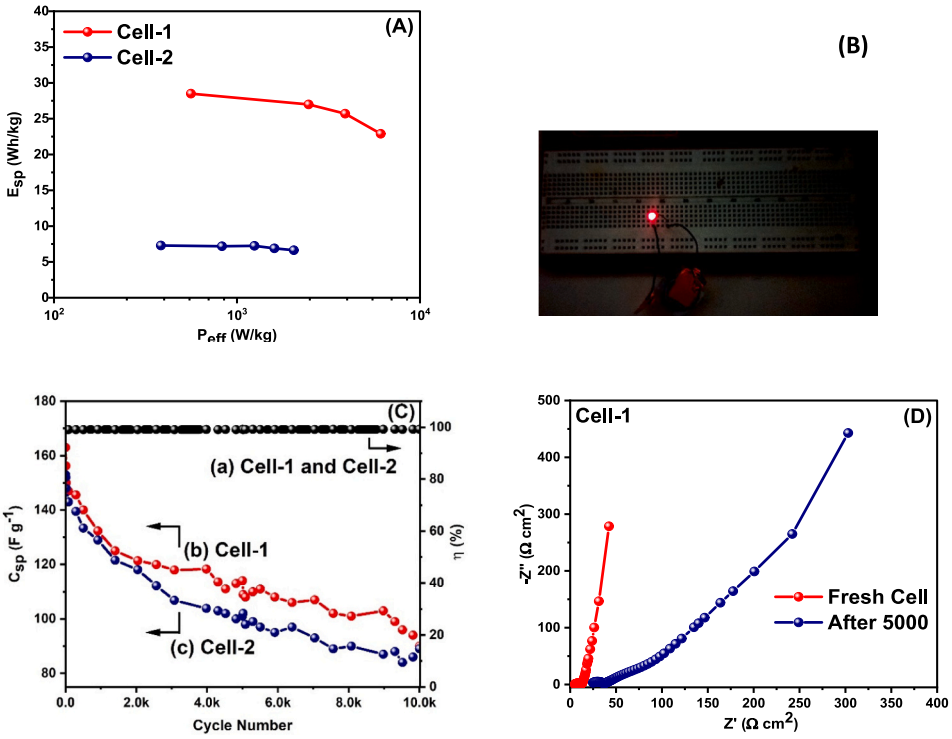

Fig. 9. (A) Comparative Ragone plots of cells (Cell-1 and Cell-2), (B) demonstration of LED glow by connecting three Cell-1 in series, (C) dependence of specific capacitance and coulombic efficiency on cycle number, (D) comparative EIS plot of GPE based cell (Cell-1) after 1st and 5000 cycles.

electrolyte ions are being inserted or removed. The columbic efficiency has been observed to be in the range of 99 % to 100 %, indicating long charge-discharge cycling stability Fig. 9(C). Owing to Cell-1 (GPE-based) optimal performance, EIS was performed on Cell-1 after 5000 cycles. The EIS pattern demonstrated the nearly steady performance for higher numbers of charge-discharge cycles. This pattern is displayed in

Fig. 9(D), which indicates that there is not much divergence across higher cycles.

4. Conclusions

By employing both chemical ($ZnCl_2$) and physical (CO_2 gas) activation procedures, asparagus biomass waste has been converted into porous activated carbon powder. The optimized carbon powder showed high BET specific surface area and hierarchical porous structure/network with appropriate content of micro-and meso- porosity as indicated by BET surface area/porosity analysis. PXRD and micro-Raman measurements confirmed the amorphous nature of the carbon powder. The hierarchical porosity of the activated carbon and the presence of heteroatom traces in the carbon matrix were shown by the SEM/EDS analysis. It has been determined that the GPE film is a superior EDLC electrolyte due to its broad electrochemical stability window of around 4.5 V vs Ag/Ag^+ as well as significant ionic conductivity of approximately 6.3×10^{-3} S cm^{-1} at ambient temperature. Using EIS, GCD, and CV measurements, the symmetric configuration of EDLCs has been constructed and characterized. The GPE based supercapacitor has almost 2 times larger electrochemical stable voltage range in comparison with the liquid electrolyte-based supercapacitor i.e., from 0 to 2.3 V voltage range for GPE based EDLC. Comparing the GPE-based EDLC to the liquid electrolyte-based EDLC, the former has marginally better capacitive performance. The Ragone plots demonstrate that the GPE-based EDLC provides the highest specific energy (e.g., 28–29 Wh kg^{-1} at specific power of 550 W kg^{-1}). The GCD and CV analyses clearly demonstrate the superior rate capability of the GPE-based EDLC. An EDLC cell based on GPE with 99–100 % coulombic efficiency and 16 % initial capacitance fading performs steadily in long-term cycling tests up to about 10,000 charge-discharge cycles. The optimal EDLC assembly with GPE and a ~ 50 mW LED light shows that the EDLC has sufficient energy storage capacity and is suitable for real-world applications.

CRediT authorship contribution statement

Niyaz Ahmad: Writing – original draft, Methodology, Investigation, Data curation, Conceptualization. **Alessia Rinaldi:** Methodology, Investigation, Formal analysis. **Michele Sidoli:** Writing – original draft, Validation, Methodology, Investigation, Formal analysis, Data curation. **Giacomo Magnani:** Writing – original draft, Supervision, Methodology, Investigation. **Alberto Morenghi:** Software, Formal analysis, Data curation. **Silvio Scaravonati:** Software, Investigation, Formal analysis, Data curation. **Vincenzo Vezzoni:** Methodology, Investigation, Data curation. **Lorenzo Pasetti:** Writing – original draft, Investigation, Formal analysis, Data curation. **Laura Fornasini:** Supervision, Formal analysis, Data curation. **Francesca Ridi:** Writing – original draft, Investigation, Formal analysis, Data curation. **Chiara Milanese:** Supervision, Project administration, Funding acquisition. **Mauro Riccò:** Supervision, Project administration, Funding acquisition. **Daniele Pontiroli:** Writing – original draft, Supervision, Project administration, Funding acquisition, Conceptualization.

Declaration of competing interest

The authors declare that they have no known competing financial interests or personal relationships that could have appeared to influence the work reported in this paper.

Data availability

Data will be made available on request.

Acknowledgements

In this publication was involved a researcher with a research contract co-financed by the European Union - PON Research and Innovation 2014-2020 pursuant to art. 24, paragraph 3, lett. a), of Law 30 December 2010, n. 240 and subsequent amendments and of the D.M. 10 August 2021 no. 1062. We acknowledge and thank Cariplo Foundation (project number 2019-2152, 'Gaining health and energy from Lombard agrifood waste') and the National Recovery and Resilience Plan (NRRP), Award Number 0001052, Mission 04 Component 2 Investment 1.5 – NextGenerationEU, call for tender n. 3277 dated 30/12/2021 (Award Number: 0001052 dated 23/06/2022) for the financial support. We also acknowledge I.I.S.S. Carlo Emilio Gadda at Fornovo di Taro (Parma, Italy) for providing scanning electron microscopy facility.

Appendix A. Supplementary data

Supplementary data to this article can be found online at https://doi.org/10.1016/j.est.2024.113267.

References

[1] P. Simon, Y. Gogotsi, Materials for electrochemical capacitors, Nat. Mater. (2008) 845–854, https://doi.org/10.1038/nmat2297, 2008 7:11 7.
[2] B.E. Conway, Electrochemical Supercapacitors: Scientific Fundamentals and Technological Applications, 1999, https://doi.org/10.1007/978-1-4757-3058-6.
[3] J. Xu, Q. Gao, Y. Zhang, Y. Tan, W. Tian, L. Zhu, L. Jiang, Preparing two-dimensional microporous carbon from Pistachio nutshell with high areal capacitance as supercapacitor materials, Scientific Reports (2014) 1–6, https://doi.org/10.1038/srep05545, 2014 4:1 4.
[4] L. He, X.Q. Zhang, A.H. Lu, Two-dimensional carbon-based porous materials: synthesis and applications, Acta Phys. -Chim. Sin. 33 (2017) 709–728, https://doi.org/10.3866/PKU.WHXB201612201.
[5] J. Chmiola, G. Yushin, Y. Gogotsi, C. Portet, P. Simon, P.L. Taberna, Anomalous increase in carbon at pore sizes less than 1 nanometer, Science 313 (2006) (1979) 1760–1763, https://doi.org/10.1126/science.1132195.
[6] R. Wu, J. Sun, C. Xu, H. Chen, MgCo2O4-based electrode materials for electrochemical energy storage and conversion: a comprehensive review, Sustain. Energy Fuel 5 (2021) 4807–4829, https://doi.org/10.1039/D1SE00909E.
[7] X. Du, X. Ren, C. Xu, H. Chen, Recent advances on the manganese cobalt oxides as electrode materials for supercapacitor applications: a comprehensive review, J. Energy Storage 68 (2023) 107672, https://doi.org/10.1016/J.EST.2023.107672.
[8] Y. Liu, X. Du, Y. Li, E. Bao, X. Ren, H. Chen, X. Tian, C. Xu, Nanosheet-assembled porous MnCo2O4.5 microflowers as electrode material for hybrid supercapacitors and lithium-ion batteries, J. Colloid Interface Sci. 627 (2022) 815–826, https://doi.org/10.1016/J.JCIS.2022.07.105.
[9] E. Bao, X. Ren, R. Wu, X. Liu, H. Chen, Y. Li, C. Xu, Porous MgCo2O4 nanoflakes serve as electrode materials for hybrid supercapacitors with excellent performance, J. Colloid Interface Sci. 625 (2022) 925–935, https://doi.org/10.1016/J.JCIS.2022.06.098.
[10] J. Sun, C. Xu, H. Chen, A review on the synthesis of CuCo2O4-based electrode materials and their applications in supercapacitors, J. Mater. 7 (2021) 98–126, https://doi.org/10.1016/J.JMAT.2020.07.013.
[11] J. Liu, Z. Khanam, S. Ahmed, H. Wang, T. Wang, S. Song, A study of low-temperature solid-state supercapacitors based on Al-ion conducting polymer electrolyte and graphene electrodes, J. Power Sources 488 (2021) 229461–229475, https://doi.org/10.1016/j.jpowsour.2021.229461.
[12] J. Liu, Z. Khanam, S. Ahmed, T. Wang, H. Wang, S. Song, Flexible antifreeze Zn-ion hybrid supercapacitor based on gel electrolyte with graphene electrodes, Appl. Mater. Interfaces 13 (2021) 16454–16468, https://doi.org/10.1021/acsami.1c02242.
[13] Y. Wang, Z. Shi, Y. Huang, Y. Ma, C. Wang, M. Chen, Y. Chen, Supercapacitor devices based on graphene materials, J. Phys. Chem. C 113 (2009) 13103–13107, https://doi.org/10.1021/jp902214f.
[14] L. Chen, X. Xu, L. Wan, G. Zhu, Y. Li, T. Lu, M.D. Albaqami, L. Pan, Y. Yamauchi, Carbon-incorporated Fe3O4 nanoflakes: high-performance faradaic materials for hybrid capacitive deionization and supercapacitors, Mater. Chem. Front. 5 (2021) 3480–3488, https://doi.org/10.1039/d0qm00946f.
[15] C. Merino, P. Soto, E. Vilaplana-Ortego, J.M. Gomez De Salazar, F. Pico, J.M. Rojo, Carbon nanofibres and activated carbon nanofibres as electrodes in supercapacitors, Carbon N Y 43 (2005) 551–557, https://doi.org/10.1016/j.carbon.2004.10.018.
[16] E. Frackowiak, F. Beguin, Carbon materials for the electrochemical storage of energy in capacitors, 2001, https://doi.org/10.1016/S0008-6223(00)00183-4.
[17] J. Gamby, P.L. Taberna, P. Simon, J.F. Fauvarque, M. Chesneau, Studies and characterisations of various activated carbons used for carbon/carbon supercapacitors, J. Power Sources 101 (2001) 109–116, https://doi.org/10.1016/S0378-7753(01)00707-8.
[18] S. Scaravonati, M. Sidoli, G. Magnani, A. Morenghi, M. Canova, J.H. Kim, M. Riccò, D. Pontiroli, Combined capacitive and electrochemical charge storage mechanism in high-performance graphene-based lithium-ion batteries, Mater. Today Energy 24 (2022) 100928, https://doi.org/10.1016/J.MTENER.2021.100928.

[19] L. Fornasini, S. Scaravonati, G. Magnani, A. Morenghi, M. Sidoli, D. Bersani, G. Bertoni, L. Aversa, R. Verucchi, M. Riccò, P.P. Lottici, D. Pontiroli, In situ decoration of laser-scribed graphene with TiO2 nanoparticles for scalable high-performance micro-supercapacitors, Carbon N Y 176 (2021) 296–306, https://doi.org/10.1016/J.CARBON.2021.01.129.
[20] A. Morenghi, S. Scaravonati, G. Magnani, M. Sidoli, L. Aversa, R. Verucchi, G. Bertoni, M. Riccò, D. Pontiroli, Asymmetric supercapacitors based on nickel decorated graphene and porous graphene electrodes, Electrochim. Acta 424 (2022) 140626, https://doi.org/10.1016/J.ELECTACTA.2022.140626.
[21] Mohit, N. Yadav, S.A. Hashmi, High energy density solid-state supercapacitors based on porous carbon electrodes derived from pre-treated bio-waste precursor sugarcane bagasse, J. Energy Storage 55 (2022) 105421, https://doi.org/10.1016/J.EST.2022.105421.
[22] Z. Song, L. Miao, L. Li, D. Zhu, L. Gan, M. Liu, A robust strategy of solvent choice to synthesize optimal nanostructured carbon for efficient energy storage, Carbon N Y 180 (2021) 135–145, https://doi.org/10.1016/j.carbon.2021.04.078.
[23] H. Duan, Z. Song, L. Miao, L. Li, D. Zhu, L. Gan, M. Liu, Unraveling the role of solvent–precursor interaction in fabricating heteroatomic carbon cathode for high-energy-density Zn-ion storage, J. Mater. Chem. A Mater. 10 (2022) 9837–9847, https://doi.org/10.1039/D2TA00754A.
[24] W. Du, L. Miao, Z. Song, X. Zheng, Y. Lv, D. Zhu, L. Gan, M. Liu, Kinetics-driven design of 3D VN/MXene composite structure for superior zinc storage and charge transfer, J. Power Sources 536 (2022) 231512, https://doi.org/10.1016/j.jpowsour.2022.231512.
[25] N. Yadav, M.K. Singh, N. Yadav, S.A. Hashmi, High performance quasi-solid-state supercapacitors with peanut-shell-derived porous carbon, J. Power Sources 402 (2018) 133–146, https://doi.org/10.1016/J.JPOWSOUR.2018.09.032.
[26] C. Zequine, C.K. Ranaweera, Z. Wang, S. Singh, P. Tripathi, O.N. Srivastava, B. Kumar Gupta, K. Ramasamy, P.K. Kahol, P.R. Dvornic, R.K. Gupta, High performance and flexible supercapacitors based on carbonized bamboo fibers for wide temperature applications OPEN, Sci. Rep. 6 (2016), https://doi.org/10.1038/srep31704.
[27] L. Zhang, J. Jiang, N. Holm, F. Chen, Mini-chunk biochar supercapacitors, J. Appl. Electrochem. 44 (2014) 1145–1151, https://doi.org/10.1007/S10800-014-0726-7/FIGURES/9.
[28] F.R. Bevlá, D.P. Rico, A.F.M. Gomis, Activated carbon from almond shells. Chemical activation. 1. Activating reagent selection and variables influence, Ind. Eng. Chem. Prod. Res. Dev. 23 (1984) 266–269, https://doi.org/10.1021/i300014a019.
[29] W. Lu, D.D.L. Chung, Mesoporous activated carbon filaments, Carbon N Y 35 (1997) 427–430, https://doi.org/10.1016/S0008-6223(97)89614-5.
[30] M. Suleman, Y. Kumar, S.A. Hashmi, Flexible electric double-layer capacitors fabricated with micro−/mesoporous carbon electrodes and plastic crystal incorporated gel polymer electrolytes containing room temperature ionic liquids, J. Solid State Electrochem. 19 (2015) 1347–1357, https://doi.org/10.1007/s10008-014-2731-5.
[31] M.R. Jisha, Y.J. Hwang, J.S. Shin, K.S. Nahm, T. Prem Kumar, K. Karthikeyan, N. Dhanikaivelu, D. Kalpana, N.G. Renganathan, A.M. Stephan, Electrochemical characterization of supercapacitors based on carbons derived from coffee shells, Mater. Chem. Phys. 115 (2009) 33–39, https://doi.org/10.1016/j.matchemphys.2008.11.010.
[32] C. Peng, X.-B. Yan, R.-T. Wang, J.-W. Lang, Y.-J. Ou, Q.-J. Xue, Promising activated carbons derived from waste tea-leaves and their application in high performance supercapacitors electrodes, Electrochim. Acta 87 (2013) 401–408, https://doi.org/10.1016/j.electacta.2012.09.082.
[33] M.-C. Liu, L.-B. Kong, P. Zhang, Y.-C. Luo, L. Kang, Porous wood carbon monolith for high-performance supercapacitors, Electrochim. Acta 60 (2012) 443–448, https://doi.org/10.1016/j.electacta.2011.11.100.
[34] D. Pontiroli, S. Scaravonati, G. Magnani, L. Fornasini, D. Bersani, G. Bertoni, C. Milanese, A. Girella, F. Ridi, R. Verucchi, L. Mantovani, A. Malcevschi, M. Riccò, Super-activated biochar from poultry litter for high-performance supercapacitors, Microporous Mesoporous Mater. 285 (2019) 161–169, https://doi.org/10.1016/J.MICROMESO.2019.05.002.
[35] W. Lu, R. Hartman, L. Qu, L. Dai, Nanocomposite electrodes for high-performance supercapacitors, J. Phys. Chem. Lett. 2 (2011) 655–660, https://doi.org/10.1021/jz200104n.
[36] F.C. Wu, R.L. Tseng, C.C. Hu, C.C. Wang, Effects of pore structure and electrolyte on the capacitive characteristics of steam- and KOH-activated carbons for supercapacitors, J. Power Sources 144 (2005) 302–309, https://doi.org/10.1016/J.JPOWSOUR.2004.12.020.
[37] A. Omri, M. Benzina, N. Ammar, Preparation, modification and industrial application of activated carbon from almond shell, J. Ind. Eng. Chem. 19 (2013) 2092–2099, https://doi.org/10.1016/j.jiec.2013.03.025.
[38] X. Chen, Y. Gu, X. Zhou, Y. Zhang, Asparagus stem as a new lignocellulosic biomass feedstock for anaerobic digestion: increasing hydrolysis rate, methane production and biodegradability by alkaline pretreatment, Bioresour. Technol. 164 (2014) 78–85, https://doi.org/10.1016/J.BIORTECH.2014.04.070.
[39] M. Qiu, H. Jiang, G. Ren, J. Huang, X. Wang, Effect of chitosan coatings on postharvest green asparagus quality, Carbohydr. Polym. 92 (2013) 2027–2032, https://doi.org/10.1016/j.carbpol.2012.11.070.
[40] Food and Agriculture Organisation of the United Nations, FAO Statistics. https://www.fao.org/faostat/en/#data, 2024 (accessed June 5, 2024).
[41] Eurostat, https://ec.europa.eu/. https://ec.europa.eu/eurostat/web/main/home, 2024 (accessed October 9, 2023).
[42] B. Santiago, G. Feijoo, M.T. Moreira, S. González-García, Identifying the sustainability route of asparagus co-product extraction: from waste to bioactive compounds, Food Bioprod. Process. 129 (2021) 176–189, https://doi.org/10.1016/J.FBP.2021.08.005.
[43] International Monetary Fund, Statistics Dept., Direction of Trade Statistics Yearbook, 2012, https://doi.org/10.5089/9781616354046.042.
[44] C. Lin, J.A. Ritter, B.N. Popov, Development of carbon-metal oxide supercapacitors from sol-gel derived carbon-ruthenium xerogels, J. Electrochem. Soc. 146 (1999) 3155–3160, https://doi.org/10.1149/1.1392448.
[45] C. Zhong, Y. Deng, W. Hu, D. Sun, X. Han, J. Qiao, J. Zhang, Electrolytes for Electrochemical Supercapacitors, 2016, https://doi.org/10.1201/b21497.
[46] N. Yadav, S.A. Hashmi, Energy enhancement of quasi-solid-state supercapacitors based on a non-aqueous gel polymer electrolyte via a synergistic effect of dual redox additives diphenylamine and potassium iodide, J. Mater. Chem. A Mater. 8 (2020) 18266–18279, https://doi.org/10.1039/D0TA06331B.
[47] C. Zhong, Y. Deng, W. Hu, J. Qiao, L. Zhang, J. Zhang, A review of electrolyte materials and compositions for electrochemical supercapacitors, Chem. Soc. Rev. 44 (2015) 7484–7539, https://doi.org/10.1039/C5CS00303B.
[48] K. Karuppasamy, J. Theerthagiri, D. Vikraman, C.J. Yim, S. Hussain, R. Sharma, T. Maiyalagan, J. Qin, H.S. Kim, Ionic Liquid-Based Electrolytes for Energy Storage Devices: A Brief Review on Their Limits and Applications, Polymers 12 (2020) 918, https://doi.org/10.3390/POLYM12040918.
[49] A. Brandt, S. Pohlmann, A. Varzi, A. Balducci, S. Passerini, Ionic liquids in supercapacitors, MRS Bull. 38 (2013) 554–559, https://doi.org/10.1557/MRS.2013.151.
[50] S.A. Hashmi, N. Yadav, M.K. Singh, Polymer Electrolytes for Supercapacitor and Challenges, Polymer Electrolytes: Characterization Techniques and Energy Applications, 2019, pp. 231–297, https://doi.org/10.1002/9783527805457.CH9.
[51] C. Zhao, W. Zheng, A review for aqueous electrochemical supercapacitors, Front. Energy Res. 3 (2015) 128918, https://doi.org/10.3389/FENRG.2015.00023/BIBTEX.
[52] A.M. Stephan, Review on gel polymer electrolytes for lithium batteries, Eur. Polym. J. 42 (2006) 21–42, https://doi.org/10.1016/J.EURPOLYMJ.2005.09.017.
[53] L. Balo, Shalu, H. Gupta, V. Kumar Singh, R. Kumar Singh, Flexible gel polymer electrolyte based on ionic liquid EMIMTFSI for rechargeable battery application, Electrochim. Acta 230 (2017) 123–131, https://doi.org/10.1016/J.ELECTACTA.2017.01.177.
[54] A.A. Hor, S.A. Hashmi, Optimization of hierarchical porous carbon derived from a biomass pollen-cone as high-performance electrodes for supercapacitors, Electrochim. Acta 356 (2020) 136826, https://doi.org/10.1016/J.ELECTACTA.2020.136826.
[55] J. Rouquerol, P. Llewellyn, F. Rouquerol, Characterization of Porous Solids VII, in: Philip Llewellyn, Francisco Rodríguez Reinoso, Jean Rouqerol, Nigel Seaton (Eds.), Proceedings of the 7th International Symposium on the Characterization of Porous Solids (COPS-VII), Amsterdam and Oxford, 2007, pp. 49–56.
[56] Book of Standards Volume: 09.01, D6556 Standard Test Method for Carbon Black-Total and External Surface Area by Nitrogen Adsorption, 2021, https://doi.org/10.1520/D6556-21.
[57] P. Tarazona, U. Marini Bettolo Marconi, R. Evans, H.H. Wills, Phase equilibria of fluid interfaces and confined fluids, Mol. Phys. 60 (2006) 573–595, https://doi.org/10.1080/00268978700100381.
[58] P. Tarazona, Free-energy density functional for hard spheres, Phys. Rev. A (Coll Park) 31 (1985) 2672–2679, https://doi.org/10.1103/PhysRevA.31.2672.
[59] M. Thommes, K. Kaneko, A.V. Neimark, J.P. Olivier, F. Rodriguez-Reinoso, J. Rouquerol, K.S.W. Sing, Physisorption of gases, with special reference to the evaluation of surface area and pore size distribution (IUPAC technical report), Pure Appl. Chem. 87 (2015) 1051–1069, https://doi.org/10.1515/pac-2014-1117.
[60] N. Yadav, Promila Ritu, S.A. Hashmi, Hierarchical porous carbon derived from eucalyptus-bark as a sustainable electrode for high-performance solid-state supercapacitors, Sustain. Energy Fuel 4 (2020) 1730–1746, https://doi.org/10.1039/C9SE00812H.
[61] H. Marsh, F. Rodríguez-Reinoso, Activated Carbon, Elsevier, 2006, https://doi.org/10.1016/B978-0-08-044463-5.X5013-4.
[62] G. Shao, Y. Lu, F. Wu, C. Yang, F. Zeng, Q. Wu, Graphene oxide: the mechanisms of oxidation and exfoliation, J. Mater. Sci. 47 (2012) 4400–4409, https://doi.org/10.1007/s10853-012-6294-5.
[63] N. Bandara, Y. Esparza, J. Wu, Graphite oxide improves adhesion and water resistance of canola protein-graphite oxide hybrid adhesive OPEN, Sci. Rep. 7 (2017), https://doi.org/10.1038/s41598-017-11966-8.
[64] K. Zhang, Y. Zhang, S. Wang, Enhancing thermoelectric properties of organic composites through hierarchical nanostructures, Scientific Reports (2013) 1–7, https://doi.org/10.1038/srep03448, 2013 3:1 3.
[65] Z.Q. Li, C.J. Lu, Z.P. Xia, Y. Zhou, Z. Luo, X-ray diffraction patterns of graphite and turbostratic carbon, Carbon N Y 45 (2007) 1686–1695, https://doi.org/10.1016/J.CARBON.2007.03.038.
[66] F. Tuinstra, J.L. Koenig, Raman spectrum of graphite, J. Chem. Phys. 53 (1970) 1126–1130, https://doi.org/10.1063/1.1674108.
[67] A. Sadezky, H. Muckenhuber, H. Grothe, R. Niessner, U. Pöschl, Raman microspectroscopy of soot and related carbonaceous materials: spectral analysis and structural information, Carbon N Y 43 (2005) 1731–1742, https://doi.org/10.1016/J.CARBON.2005.02.018.
[68] A.C. Ferrari, D.M. Basko, Raman spectroscopy as a versatile tool for studying the properties of graphene, Nat. Nanotechnol. (2013) 235–246, https://doi.org/10.1038/nnano.2013.46, 2013 8:4 8.
[69] A. Ferrari, J. Robertson, Interpretation of Raman spectra of disordered and amorphous carbon, Phys. Rev. B 61 (2000) 14095, https://doi.org/10.1103/PhysRevB.61.14095.

[70] N. Yadav, N. Yadav, S.A. Hashmi, Ionic liquid incorporated, redox-active blend polymer electrolyte for high energy density quasi-solid-state carbon supercapacitor, J. Power Sources 451 (2020) 227771, https://doi.org/10.1016/j.jpowsour.2020.227771.
[71] Y. Kumar, G.P. Pandey, S.A. Hashmi, Gel polymer electrolyte based electrical double layer capacitors: comparative study with multiwalled carbon nanotubes and activated carbon electrodes, J. Phys. Chem. C 116 (2012) 26118–26127, https://doi.org/10.1021/jp305128z.
[72] R. de Levie, On porous electrodes in electrolyte solutions. I. Capacitance effects, Electrochim. Acta 8 (1963) 751–780, https://doi.org/10.1016/0013-4686(63)80042-0.
[73] S.T. Senthilkumar, R.K. Selvan, Y.S. Lee, J.S. Melo, Electric double layer capacitor and its improved specific capacitance using redox additive electrolyte, J. Mater. Chem. A Mater. 1 (2012) 1086–1095, https://doi.org/10.1039/C2TA00210H.
[74] P.L. Taberna, P. Simon, J.F. Fauvarque, Electrochemical characteristics and impedance spectroscopy studies of carbon-carbon supercapacitors, J. Electrochem. Soc. 150 (2003) A292, https://doi.org/10.1149/1.1543948.
[75] John R. Miller, Pulse Power Performance of Electrochemical Capacitors: Technical Status of Present Commercial Devices: Technical Status of Present Commercial Devices, 8th International Seminar on Double Layer Capacitors and Similar Energy Storage Devices, 1998.
[76] R.L. Spyker, R.M. Nelms, Classical equivalent circuit parameters for a double-layer capacitor, IEEE Trans Aerosp Electron Syst (2000) 829–836, https://doi.org/10.1109/7.869502.
[77] P. Navalpotro, J. Palma, M. Anderson, R. Marcilla, High performance hybrid supercapacitors by using para-Benzoquinone ionic liquid redox electrolyte, J. Power Sources (2015), https://doi.org/10.1016/j.jpowsour.2015.12.103.
[78] K. Adlak, R. Chandra, V.K. Vijay, K.K. Pant, Physicochemical activation and palletisation of Azadirachta indica wood carbons for increased biomethane adsorbed energy storage, J. Anal. Appl. Pyrolysis 155 (2021) 105102, https://doi.org/10.1016/J.JAAP.2021.105102.
[79] L. Huang, Q. Wu, S. Liu, S. Yu, A.J. Ragauskas, Solvent-free production of carbon materials with developed pore structure from biomass for high-performance supercapacitors, Ind. Crop. Prod. 150 (2020) 112384, https://doi.org/10.1016/J.INDCROP.2020.112384.
[80] B. Jia, Q. Mian, D. Wu, T. Wang, Heteroatoms self-doped porous carbon from cottonseed meal using K2CO3 as activator and DES electrolyte for supercapacitor with high energy density, Mater. Today Chem. 24 (2022) 100828, https://doi.org/10.1016/J.MTCHEM.2022.100828.
[81] D.A. Khuong, T.T. Kieu, Y. Nakaoka, T. Tsubota, D. Tashima, H.N. Nguyen, D. Tanaka, The investigation of activated carbon by K2CO3 activation: micropores- and macropores-dominated structure, Chemosphere 299 (2022) 134365, https://doi.org/10.1016/J.CHEMOSPHERE.2022.134365.
[82] E. Taer, D. Afdal Yusra, A. Amri, R. Taslim Awitdrus, Agustino Apriwandi, A. Putri, The synthesis of activated carbon made from banana stem fibers as the supercapacitor electrodes, Mater. Today Proc. 44 (2021) 3346–3349, https://doi.org/10.1016/J.MATPR.2020.11.645.
[83] Z. Xiao, W. Chen, K. Liu, P. Cui, D. Zhan, Electrochemical science porous biomass carbon derived from peanut shells as electrode materials with enhanced electrochemical performance for supercapacitors, Int. J. Electrochem. Sci. 13 (2018) 5370–5381, https://doi.org/10.20964/2018.06.54.
[84] D. Wang, S. Liu, G. Fang, G. Geng, J. Ma, From Trash to Treasure: Direct Transformation of Onion Husks into Three-Dimensional Interconnected Porous Carbon Frameworks for High-Performance Supercapacitors in Organic Electrolyte, 2016, https://doi.org/10.1016/j.electacta.2016.09.053.
[85] J. Hou, C. Cao, X. Ma, F. Idrees, B. Xu, X. Hao, W. Lin, From Rice Bran to High Energy Density Supercapacitors: A New Route to Control Porous Structure of 3D Carbon, Scientific Reports (2014) 1–6, https://doi.org/10.1038/srep07260, 2014 4:1 4.
[86] M. Yasir Bhat, N. Yadav, S. Hashmi, Pinecone-derived porous activated carbon for high performance all-solid-state electrical double layer capacitors fabricated with flexible gel polymer electrolytes, 2019, https://doi.org/10.1016/j.electacta.2019.02.092.
[87] A.A. Hor, S.A. Hashmi, Optimization of hierarchical porous carbon derived from a biomass pollen-cone as high-performance electrodes for supercapacitors, Electrochim. Acta 356 (2020) 136826, https://doi.org/10.1016/J.ELECTACTA.2020.136826.
[88] K. Charoensook, C.-L. Huang, H.-C. Tai, V. Venkata, K. Lanjapalli, L.-M. Chiang, S. Hosseini, Y.-T. Lin, Y.-Y. Li, Preparation of porous nitrogen-doped activated carbon derived from rice straw for high-performance supercapacitor application, 2021, https://doi.org/10.1016/j.jtice.2021.02.021.
[89] Z. Huang, C. Qin, J. Wang, L. Cao, Z. Ma, Q. Yuan, Z. Lin, P. Zhang, P. Maireles-Torres, Materials research on high-value utilization of carbon derived from tobacco waste in supercapacitors, Materials 14 (2021) 1714, https://doi.org/10.3390/ma14071714.
[90] W.-H. Qu, Y.-Y. Xu, A.-H. Lu, X.-Q. Zhang, W.-C. Li, Converting biowaste corncob residue into high value added porous carbon for supercapacitor electrodes, Bioresour. Technol. (2015), https://doi.org/10.1016/j.biortech.2015.04.005.
[91] C. Huang, T. Sun, D. Hulicova-Jurcakova, Wide electrochemical window of supercapacitors from coffee bean-derived phosphorus-rich carbons, ChemSusChem 6 (2013) 2330–2339, https://doi.org/10.1002/CSSC.201300457.
[92] M. Chen, X. Kang, T. Wumaier, J. Dou, B. Gao, Y. Han, G. Xu, Z. Liu, L. Zhang, Preparation of activated carbon from cotton stalk and its application in supercapacitor, J. Solid State Electrochem. (2013), https://doi.org/10.1007/s10008-012-1946-6.